

# 1 Diagenetic evolution of fault zones in Urgonian microporous 2 carbonates, impact on reservoir properties (Provence – SE France).

3  
4 *Irène Aubert <sup>a</sup>, Philippe Léonide <sup>a</sup>, Juliette Lamarche <sup>a</sup>, Roland Salardon <sup>a</sup>*

5  
6 *<sup>a</sup> Aix-Marseille Université, CNRS, IRD, Cerege, Um 34, 3 Place Victor Hugo (Case 67), 13331*  
7 *Marseille Cedex 03, France*

8  
9  
10 Microporous carbonate rocks form important reservoirs with permeability variability depending  
11 on sedimentary, structural and diagenetic factors. Carbonates are very sensitive to fluid-rock  
12 interactions that lead to secondary diagenetic processes like cementation and dissolution  
13 capable of modifying the reservoir properties. Focusing on fault-related diagenesis, the aim of  
14 this study is to identify impact of the fault zone on reservoir quality. This contribution focuses  
15 on two fault zones east to La Fare Anticline (SE France) cross-cutting Urgonian microporous  
16 carbonates. 122 collected samples along four transects orthogonal to fault strike were analysed.  
17 Porosity values have been measured on 92 dry plugs. Diagenetic elements were determined  
18 through the observation of 92 thin sections using polarized light microscopy,  
19 cathodoluminescence, red alizarin, SEM and stable isotopic measurements ( $\delta^{13}\text{C}$  and  $\delta^{18}\text{O}$ ).  
20 Eight different calcite cementation stages and two micrite micro-fabrics were identified. As a  
21 main result, this study highlights that the two fault zones acted as drains canalizing low-  
22 temperature fluids at their onset, and induced calcite cementation which strongly altered and  
23 modified the local reservoir properties.

## 24 1. INTRODUCTION

25 Microporous carbonates form important reservoirs (Deville de Periere et al., 2017; Lambert et  
26 al., 2006; Sallier, 2005; Volery et al., 2009), with porosity values up to 35% (Deville de Periere  
27 et al., 2011). Due to their heterogeneous properties which depends on sedimentary, structural  
28 and diagenetic factors, microporous carbonates may determine a high variability of reservoir  
29 permeability (Bruna et al., 2015; Deville de Periere et al., 2011, 2017; Eltom et al., 2018; Florida  
30 et al., 2009; Hollis et al., 2010). Moreover, fault zones in carbonates play an important role on  
31 reservoir properties (Agosta et al., 2010, 2012; Caine et al., 1996; Delle Piane et al., 2016;  
32 Ferraro et al., 2019; Knipe, 1993; Laubach et al., 2010; Rossetti et al., 2011; Sinisi et al., 2016;  
33 Solum et al., 2010; Solum and Huisman, 2016; Tondi, 2007; Wu et al., 2019). Fault zones are  
34 complex structures composed of damage zones and the fault core encompassed by the host rock  
35 (Caine et al., 1996; Chester and Logan, 1986, 1987; Hammond and Evans, 2003). Faults can  
36 act as barriers (Agosta et al., 2010; Tondi, 2007), drains (Agosta et al., 2007, 2008, 2012; Delle  
37 Piane et al., 2016; Evans et al., 1997; Molli et al., 2010; Reches and Dewers, 2005; Sinisi et al.,  
38 2016; Solum and Huisman, 2016), or mixed hydraulic behaviour zones (Matonti et al., 2012)  
39 depending on their architecture and diagenetic evolution. Because of their hydraulic properties,  
40 fault zones influence the fluid flows in the upper part of Earth's crust (Bense et al., 2013; Evans  
41 et al., 1997; Knipe, 1993; Sibson, 1994; Zhang et al., 2008), and are capable of increasing the  
42 fluid-rock interactions. Carbonates are very sensitive to these interactions, which lead to

43 diagenetic secondary processes like cementation and dissolution (Deville de Periere et al., 2017;  
44 Fournier and Borgomano, 2009; Lambert et al., 2006). Fault-related diagenesis locally modifies  
45 the initial rock properties (mineralogy and porosity), and therefore the reservoir properties  
46 (Hodson et al., 2016; Knipe, 1993; Knipe et al., 1998; Laubach et al., 2010; Woodcock et al.,  
47 2007). In case of a polyphasic fault zone, repeating fluid pathways-barriers behaviour in times  
48 leads to very complex diagenetic modifications. The initial vertical and lateral  
49 compartmentalization of microporous limestones is, therefore, accentuated by fault-related  
50 diagenesis. Hence, understanding faulting processes and diagenesis is crucial for a better  
51 exploration and production in carbonates. Urgonian microporous carbonates of Provence, are  
52 made of facies and reservoir properties analogue to Middle East microporous carbonate  
53 reservoirs (Thamama, Kharaib and Shuaiba Formations; Borgomano et al. 2002, 2013; Sallier  
54 2005; Fournier et al. 2011; Leonide et al. 2012; Léonide et al. 2014). Although Urgonian  
55 microporous carbonates of Provence are analogue to Middle East reservoirs, the analogy can  
56 be extended to other faulted microporous carbonate reservoirs. To have a better comprehension  
57 of diagenetic modifications linked to fault zones on these rocks, the aim of this paper is (i) to  
58 determine the diagenetic evolution of polyphasic fault zones; (ii) to identify their impact on  
59 reservoir properties and (iii) to link the fault evolution with the fluid flow and geodynamic  
60 history of the basin.

## 61 **2. GEOLOGICAL CONTEXT**

62 We studied two faults cross-cutting microporous Valanginian-to-Early Aptian Urgonian  
63 carbonates of the South-East Basin (Provence-SE France) deposited along the southern margin  
64 of the Vocontian Basin (Léonide et al., 2014; Masse and Fenerci Masse, 2011). The “Urgonian”  
65 platform carbonates (Masse, 1976) reached their maximum areal extension during the late  
66 Hauterivian–Early Aptian (Masse and Fenerci-Masse, 2006). From Albian to Cenomanian, the  
67 regional Durancian uplift triggered exhumation of Early Cretaceous carbonates, bauxitic  
68 deposition (Guyonnet-Benaize et al., 2010; Lavenu et al., 2013; Léonide et al., 2014; Masse  
69 and Philip, 1976; Masse, 1976), and development E-W-trending extensional faults (Guyonnet-  
70 Benaize et al., 2010; Masse and Philip, 1976). During the Late-Cretaceous times, platform  
71 environment led to a transgressive rudist platform deposition (Philip, 1970). From Late  
72 Cretaceous to Eocene, the convergence between Iberia plate and Eurasia plates (e.g. Bestani  
73 2015, and references therein) caused a regional N-S shortening (e.g. Molliex et al. 2011 and  
74 references therein). The so-called “Pyrénéo-Provençal” shortening, gave rise to E-W-trending  
75 north-verging thrust faults and ramp folds (e.g. Bestani et al. 2016, and references therein).  
76 From Oligocene to Miocene, the area underwent extension associated to Liguro-Provençal  
77 Basin opening (e.g. Demory et al. 2011). During Mio-Pliocene times, the Alpine shortening  
78 dimly impacted the studied area (Besson, 2005; Bestani, 2015), and reactivated the “Pyrénéo-  
79 Provençal” structures (Champion et al., 2000; Molliex et al., 2011).

80

81 We studied two faults pertaining to a Km-scale fault system on the E-W-trending La Fare  
82 anticline near Marseille (Fig. 1A). The southern limb of this anticline dips 25° S, and is  
83 constituted by Upper Hauterivian, Lower Barremian and Santonian rocks (Fig. 1B). The Upper  
84 Barremian carbonates are composed, from bottom to top, of a 120 m-thick calcarenitic unit  
85 with cross-beddings, a 40 m-thick massive coral-rich calcarenite unit, and an upper 10 m-thick

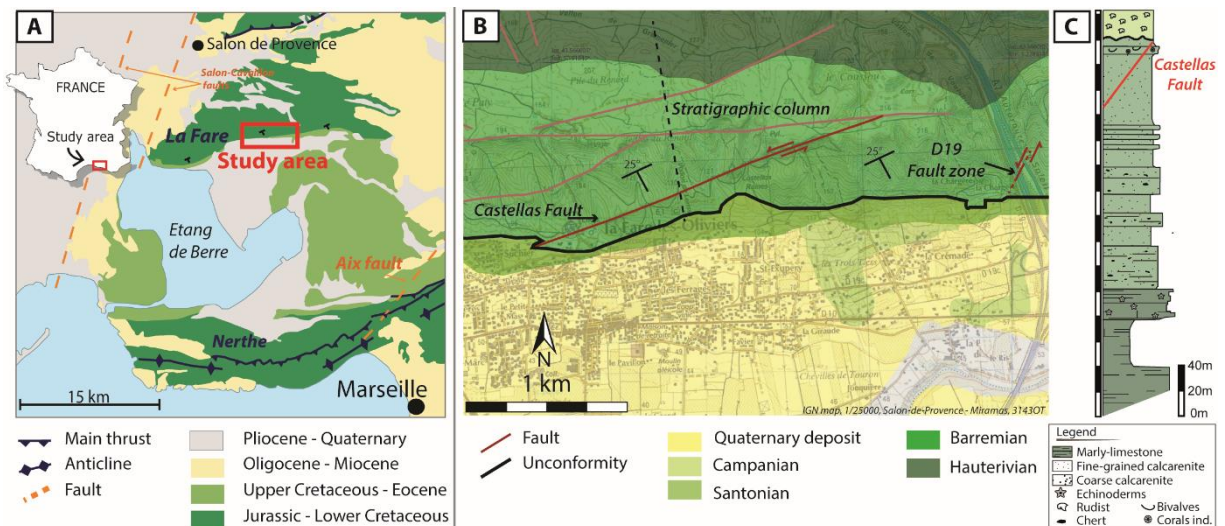
86 calcarenite unit (Masse, 1976; Matonti et al., 2012; Roche, 2008). Santonian age coarse rudist  
 87 limestones uncomfortably overlap the Barremian carbonates (Fig. 1A).

88 The Castellans fault zone is a 2.14 km-long left-lateral strike-slip fault, N060 to 070-trending  
 89 and 40° to 80°N-dipping (Fig. 2A, 2B; table 1) composed horse structures, secondary faults and  
 90 lenses (Fig. 2A, 2C; Aubert et al. (2019b)). The second investigated fault zone “D19” is  
 91 composed of 5 sub-fault zones (F1 to F5) restricted in a 50m-long extension (Fig. 2E, 2H; Table  
 92 1; (Aubert et al., 2019a)). Sub-faults are organised into two sets. The first one comprises F3 and  
 93 F4, N040 to N055-trending, 60-80°NW-dipping (orange traces on Fig. 2F). Set 2 is N030-  
 94 trending, dipping 80°E, with left-lateral strike-slip slickensides pitch 20 to 28°SW (F1, F2, F5,  
 95 red traces on Fig. 2F).

96  
 97 The internal structure of both fault zones results from three distinct tectonic events:

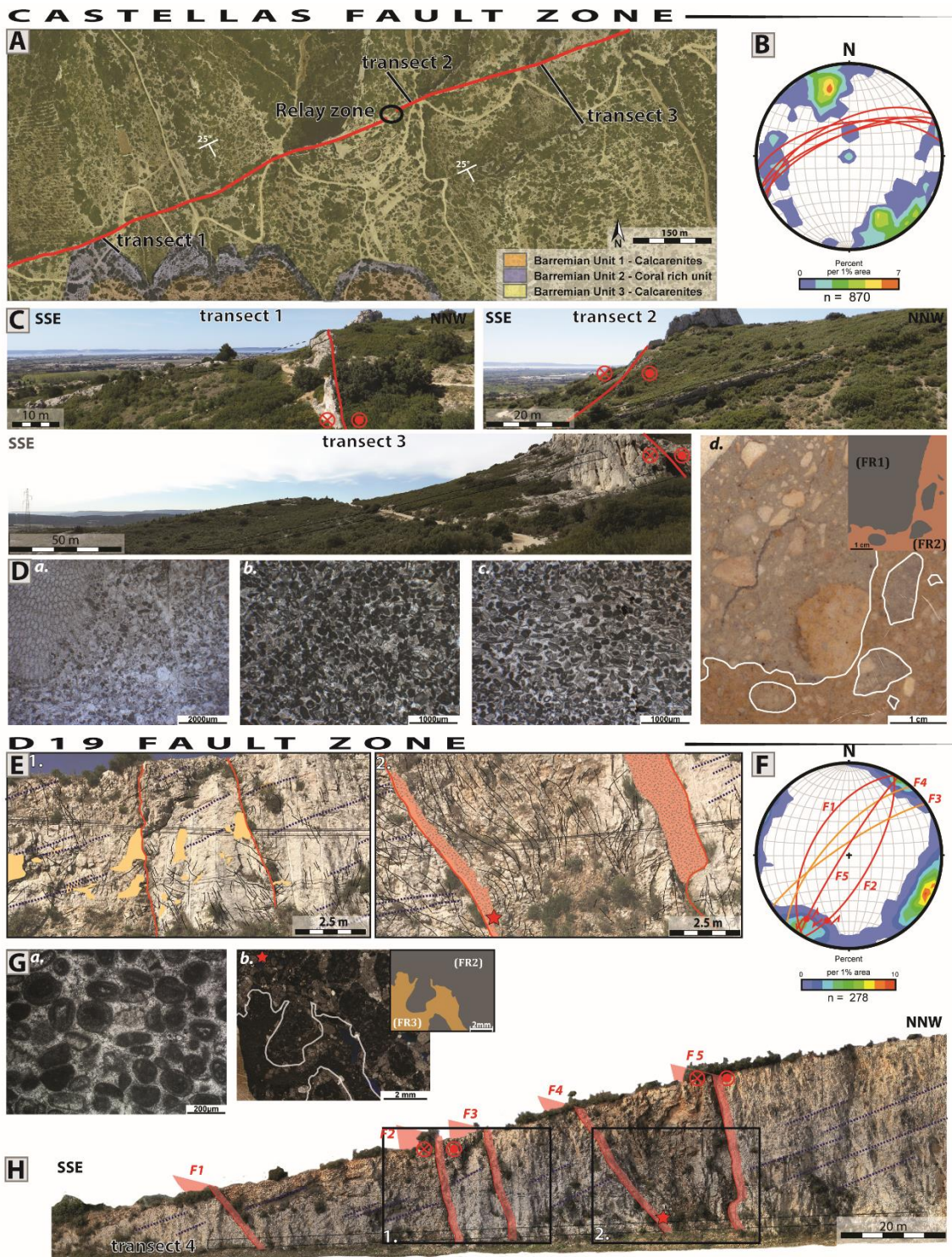
- 98 - the Durancian uplift dated as mid-Cretaceous leading to extension and to normal *en*  
 99 *echelon* normal faults. The Castellans fault nucleated during this first extensional event  
 100 and bear early dip-slip normal striations (Matonti et al., 2012),
- 101 - the Early Pyrenean compression with N000° to N170°-trending  $\sigma_H$  (see cited references  
 102 in Espurt et al. 2012) which reactivated the Castellans fault as sinistral (Matonti et al.,  
 103 2012) and led to the newly-formed strike-slip faults of the D19 outcrop (Aubert et al.,  
 104 2019a).
- 105 - the Pyrenean to Alpine folding, triggering the 25°S tilting of the strata and fault zones.  
 106 Faults of the D19 outcrop were reactivated while the Castellans fault tilting led to an  
 107 apparent present-day reverse throw (Aubert et al., 2019a).

108



109  
 110 **Figure 1** : Geological context of the study area. A: geological map of Provence, B: Simplified structural map with the  
 111 location of the Castellans fault and the stratigraphic column (black dashed line); C: Stratigraphic column of exposed  
 112 Cretaceous carbonates (modified from Roche, 2008)

113



114

115 **Figure 2** : A: Castellás fault map on aerial photo with position of the studied transects and the relay zone; B: stereographic  
 116 projections of poles to fractures (density contoured) and faults (red lines) (Allmendinger et al., 2013; Cardozo and  
 117 Allmendinger, 2013); C: Photos of transects 1 to 3; D: Photomicrographs of carbonate host-rock facies (a) transect 1 coral  
 118 rich unit, (b) transect 2 calcarenites, (c) transect 3 calcarenites and (d) fault rocks 1 and 2 (FR1 and FR2); E: Pictures of D19  
 119 outcrop F: Stereographic projections of poles to fractures (density contoured), set one faults (orange line) and set 2 faults (red  
 120 line) G: Photomicrograph of host rock facies (a) and of fault rocks (b; red stars on the pictures)); H: D19 outcrop including  
 121 the five faults F1 to F5.

122

123 **Table 1:** structural properties of the fault zones.

Fault zones	Fault	Direction	Dip	Dip direction	Pitch striation	Fault core thickness	Fault Rocks		
							FR1	FR2	FR3
Castellas	Castellas	060 - 070	40 to 80	N	14 W -	0 to 4 m	sparsely present	majoritarily present	/
D19	F1	030	56	W		20	/	<10 cm	/
	F2	029	70	E	28 S	10 to 15	/	?	variable thickness
	F3	056	80	N		0 to 15	/	?	?
	F4	042	70	W		20	/	in the clasts of FR3	variable thickness
	F5	032	85	N	20 SW	50 to 100	/	/	variable thickness

124

### 125 3. DATA BASE

126 We performed 4 transects across the Castellas Fault and the D19 Fault (Fig. 2). Transect 1 is  
 127 located along the coral rich unit 2. This lithostratigraphic unit is essentially composed of  
 128 peloidal grains and bioclasts (corals, bivalves and stromatoporidae; Fig. 2Da). Transects 2 and  
 129 3 cross-cut in unit 3, made of fine calcarenites with peloidal grains and a rich fauna  
 130 (foraminifera, bivalves, ostracods and echinoderms; Fig. 2Db, c). Transect 4 was conducted  
 131 along the D19 outcrop (Fig. 3), which exposes Barremian outer platform bioclastic calcarenite  
 132 with current ripples. The grains are mainly peloids with minor amounts of bioclasts (solidary  
 133 corals, bryozoans, bivalves and some rare miliolids; Fig. 2Ga).

134  
 135 The different tectonic events impacted the fault zone and fault core structure. Three different  
 136 fault rock types were identified in the fault core of the two investigated fault zones ( see Aubert  
 137 et al. 2019a; Matonti et al., 2012). Fault rock 1 (FR1) results from the extensional activation of  
 138 the Castellas fault during Durancian uplift. It is a cohesive breccia composed of sub-rounded to  
 139 rounded clasts from the nearby damage zone and <30% of fine-grey matrix (Fig. 2Dd). Fault  
 140 rock 2 (FR2), is linked to the strike reactivation of the Castellas fault and to the onset of D19  
 141 fault zone during the Pyrenean shortening. FR2 presents two morphologies depending on the  
 142 fault zones. Within Castellas fault, FR2 is an un-cohesive breccia with an orange/oxidized  
 143 matrix with angular to sub-rounded clasts belonging to the nearby damage zone and from FR1  
 144 (Fig. 2Dd). In the D19 fault zone, FR2 is a cohesive breccia with rounded clasts of the damage  
 145 zone and a white cemented matrix (Fig. 2Gb). Fault rock 3 (FR3) is formed by the reactivation  
 146 of D19 fault zone. The timing of D19 fault reactivation is tricky to determine as it can be related  
 147 both to Pyrenean or alpine shortening. FR3 is composed of angular to sub-angular clasts from  
 148 FR2 and from the nearby damage zone dispersed in an orange/oxidized matrix (<20%) (Fig.  
 149 2Gb).

150

### 151 4. METHODS

152 The data set comprises 122 samples, 62 from Castellas and 60 from D19 outcrops, collected  
 153 along the 4 transects. Porosity values were measured on 92 dry plugs with a Micromeritics  
 154 AccuPyc 1330 helium pycnometer. Microfacies were determined on 92 thin sections.  
 155 Impregnation with a blue-epoxy resin allowed us to decipher the different pore types. Thin  
 156 sections were coloured with a solution of hydrochloric acid, Alizarin red S and potassium  
 157 ferricyanide to distinguish carbonate minerals (calcite and dolomite). Thin sections were  
 158 analysed using cathodoluminescence to discriminate the different generation of calcite cements.

159 The paragenetic sequence was defined based on superposition and overlap principles observed  
160 on thin sections using a Technosyn Cold Cathode Luminescence Model 8200 Mk II coupled to  
161 an Olympus\_BH2 microscope and to a Zeiss\_MR C5. Micrite micro-fabric and major element  
162 composition of two samples from the fault zone, two from the host rock and 1 from the D19  
163 karst infilling were measured using PHILIPS XL30 ESEM with a beam current set at 20 kV on  
164 fresh sample surfaces and on thin sections. To determine stable carbon and oxygen isotopes  
165 ( $\delta^{13}\text{C}$  and  $\delta^{18}\text{O}$ ), 204 microsamples (<5 mg) were drilled, 194 of them were micro-drilled from  
166 polished thin sections with an 80  $\mu\text{m}$  diameter micro-sampler (Merkantec Micromill) at the VU  
167 University (Amsterdam, The Netherlands). We micro-sampled bulk rocks (57), sparitic cements  
168 (101), fault rocks (9) and micrite (27). The Bulk rock values are related to a non-selective  
169 sampling giving information on the whole rock isotopic values. These values do not capture the  
170 signature of isolated cement (Swart, 2015). Carbon and oxygen isotopic values were acquired  
171 with Thermo Finnigan Delta + mass spectrometer equipped with a GASBENCH preparation  
172 device at VU University Amsterdam. The internationally used standard IAEA-603, with official  
173 values of +2.46‰ for  $\delta^{13}\text{C}$  and -2.37‰ for  $\delta^{18}\text{O}$ , is measured as a control standard. The standard  
174 deviation (SD) of the measurements is respectively < 0.1‰ and < 0.2 ‰ for  $\delta^{13}\text{C}$  and  $\delta^{18}\text{O}$ ,  
175 respectively. Ten whole rock samples were analysed using a Gasbench II connected to a  
176 Thermo Fisher Delta V Plus mass spectrometer at the FAU University (Erlangen, Germany).  
177 Measurements were calibrated by assigning  $\delta^{13}\text{C}$  values of +1.95‰ to NBS19 and -47.3‰ to  
178 IAEA-CO9 and  $\delta^{18}\text{O}$  values of -2.20‰ to NBS19. All values are reported in per mil relative to  
179 V-PDB.

## 180 5. RESULTS

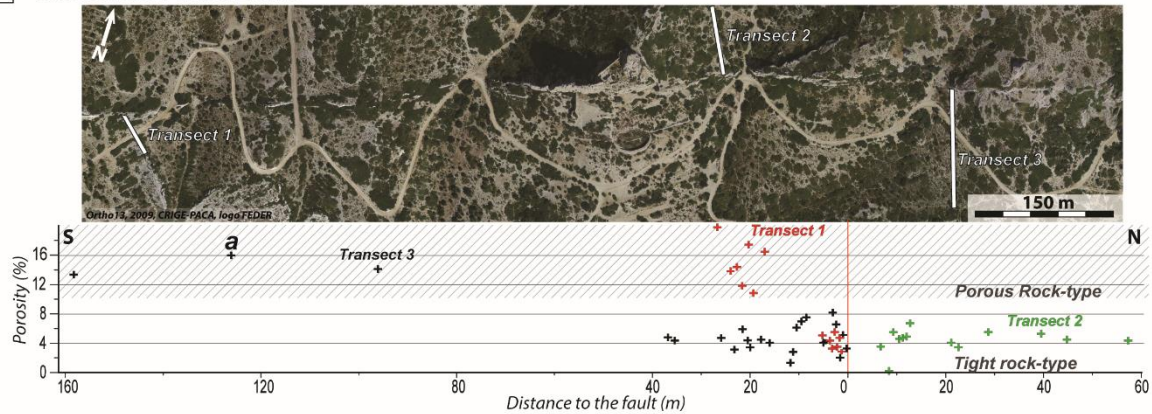
### 181 1. MICROPOROSITY AND POROSITY

182 Porosities measured on the 92 samples show a strong decrease towards the fault core (Fig. 3):  
183 dropping from more than 10% in the host carbonates (mean: 15%, SD: 2.68 for Castellás and  
184 mean 12.3%, SD: 2.52 for D19) to less than 5% within fault zones (mean: 4.8%, SD: 2.07 for  
185 Castellás and mean: 3.16%, SD: 2.35 for D19).

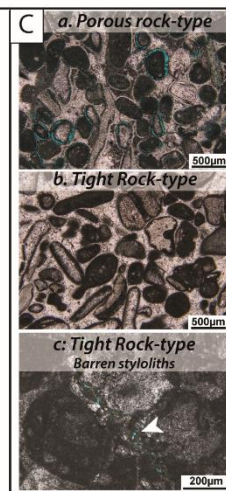
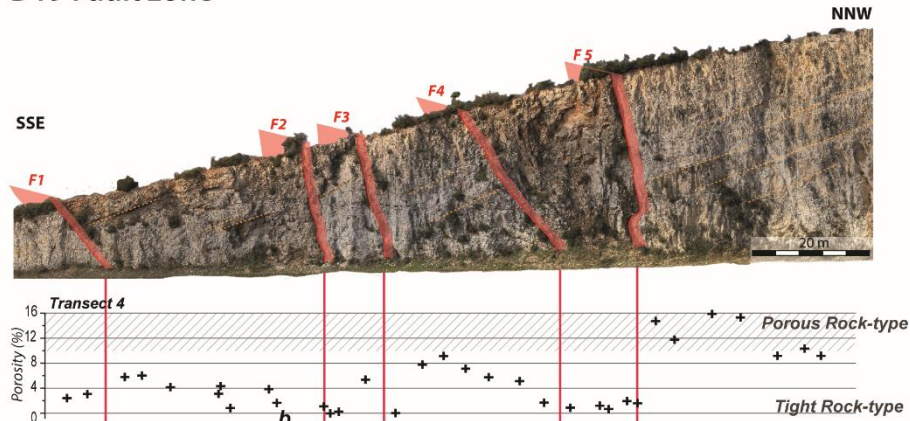
186 Along transects, some porosity variations occur as follows:

- 187 - North of the Castellás fault, along the 60 m-long transect 2 the porosity is constantly  
188 lower than 7% (mean of 4.4%, SD: 1.53; Fig. 3A).
- 189 - South of the Castellás fault, the reduced porosity zone is wider than 40 m in transect 3  
190 and 30 m in transect 1 (Fig. 3A). In a 10 m-thick zone from the fault plane, porosity  
191 reduction occurs with lower values in transect 1 (average 4.9%) than in transect 3  
192 (average 5.6%).

## A Castellás Fault zone



## B D19 Fault zone



193

194 **Figure 3:** A: Castellás fault zone aerial view (Ortho13, 2009, CRIGE-PACA, logo FEDER) and porosity values measured  
 195 along transect 1 (Red Cross), transect 2 (green cross) and transect 3 (black cross); B: porosity values measured along D19  
 196 fault zone; C: Pore types in the host rock (a) and in the fault zones (b and c).

197 In the D19 fault zone, the lowest porosity values are found in narrow zones around the faults  
 198 (less than 2 m-wide) and in the lens between F4 and F5. Though, this porosity decrease is not  
 199 homogeneous in fault zone and high values are found north of F1 and F3 (Fig. 3B).

200 Microscope observation of thin sections impregnated with blue-epoxy resin allowed to  
 201 identified a porous rock-type with  $\phi > 10\%$  mainly in micritized grains as microporosity and  
 202 moldic porosity (Fig. 3Ca), and a tight rock-type with  $\phi < 5\%$ , where the porosity is mostly  
 203 linked to barren stylolites (Fig. 3Cb, c).

## 204 2. DIAGENETIC PHASES

### 205 a. Micrite micro-fabric

206 Micritised bioclasts, ooids and peloids were observed after SEM analysed of two fault zones  
 207 samples and two host rock samples. Two micro-fabrics of micrite occur with specific crystal  
 208 shape, sorting and contacts according to Fournier et al. (2011). Within both fault zones, the  
 209 micrite is tight, with compact subhedral mosaic crystals of less than 10  $\mu\text{m}$ -wide (MF1; Fig.  
 210 4A, B). In the host rock, the micrite is loosely packed, and partially coalescent with punctate  
 211 rarely serrate, subhedral to euhedral crystals of less than 5  $\mu\text{m}$ -wide (MF3; Fig. 4C, D, E). MF1  
 212 correlates with low porosity values ( $< 5\%$ ), while MF3 with higher porosity ( $> 10\%$ ).

213       **b. Diagenetic cements**

214 Eight different cement stages were identified (Fig. 5). The red stain links to Alizarin Red S  
215 coloration and shows that all visible cements made of calcite, which exhibit variable  
216 characteristics (morphology, luminescence, size and location).

217 The first two cement phases occur in both fault zones. The first cement (C0) is non-luminescent  
218 isopachous calcite of constant thickness (~10 µm) around grains (Fig. 5A). The second cement  
219 (C1) is divided in two sub-phases: a non-luminescent calcite, C1a, with a crystal size ranging  
220 from 50 µm to more than 200 µm, a dog-tooth morphology in intergranular spaces, and a bright  
221 luminescence calcite, C1b, covering C1a with a maximum thickness of 100 µm (Fig. 5A, B,  
222 D, G). C1b also fills micro-porosity in micritised grains (Fig. 5B). C1b areal occurrence  
223 strongly increases in Castellás fault zone.

224



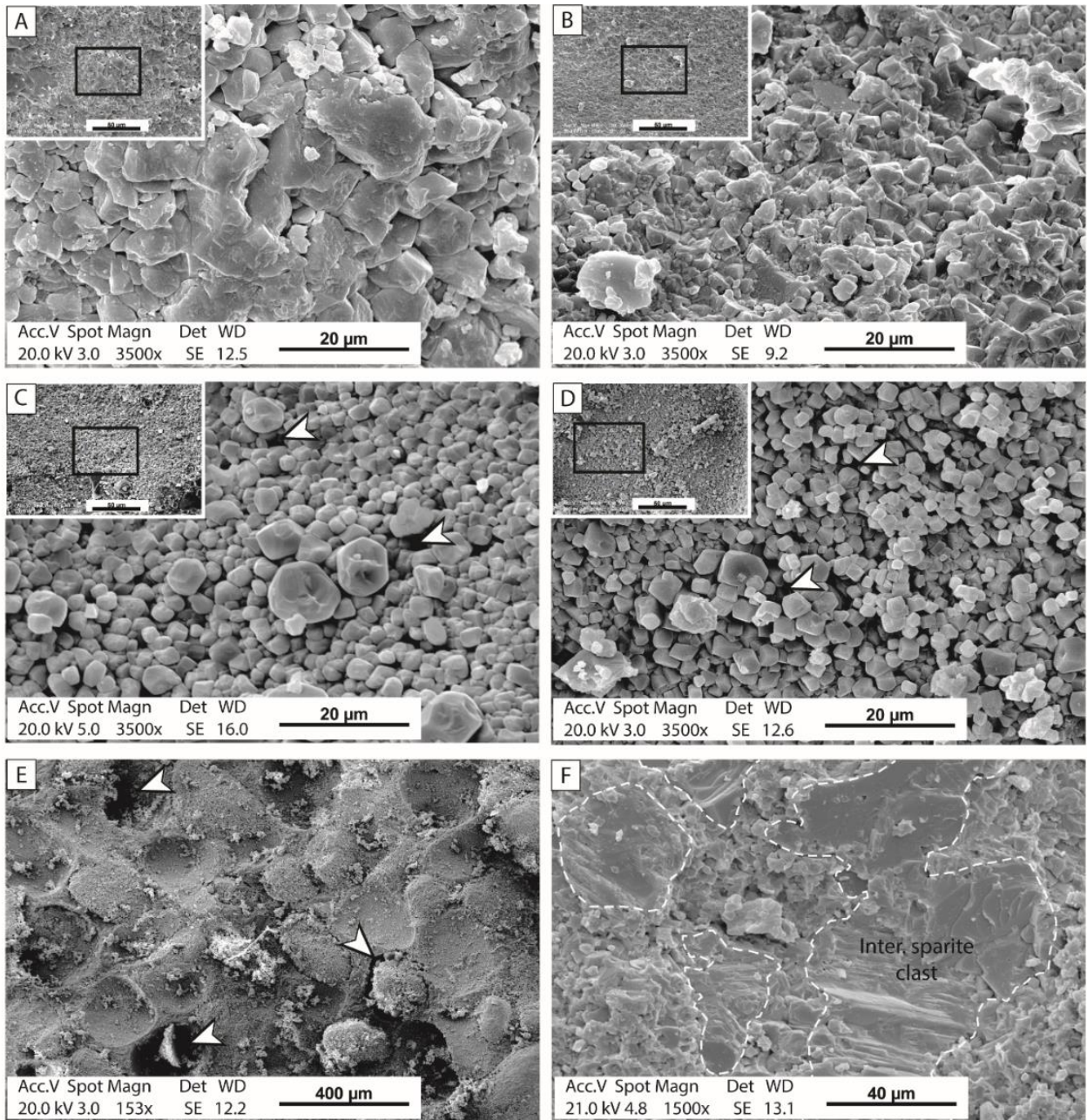


**Figure 4 :** MEB pictures of micrite micro-fabric and microporosity (white arrows); A. MF1 micrite micro-fabric in Castellás fault zone (2.5 m to fault plane); B. MF1 micrite micro-fabric within D19 fault zones (2 m away from F5 fault plane); C. MF3 micrite micro-fabric within Castellás host rock (188 m away from the fault plane); D. MF3 micrite micro-fabric within D19 host rock (95 m away from F5 fault plane); E. D19 host rock moldic porosity; F. Karst infilling.

225

226 Five cements or replacive phases extensively occur in the Castellás sector and rarely in the D19  
 227 outcrop:

- 228 - C2 is a sparitic cement, with dull-orange luminescent crystals sized of maximum 100  
 229 µm only found in veins of the fault core (Fig. 5B). SEM measurements show the Si and  
 230 Al in the C2 veins. Most of Si crystals are automorphic and have black luminescence.

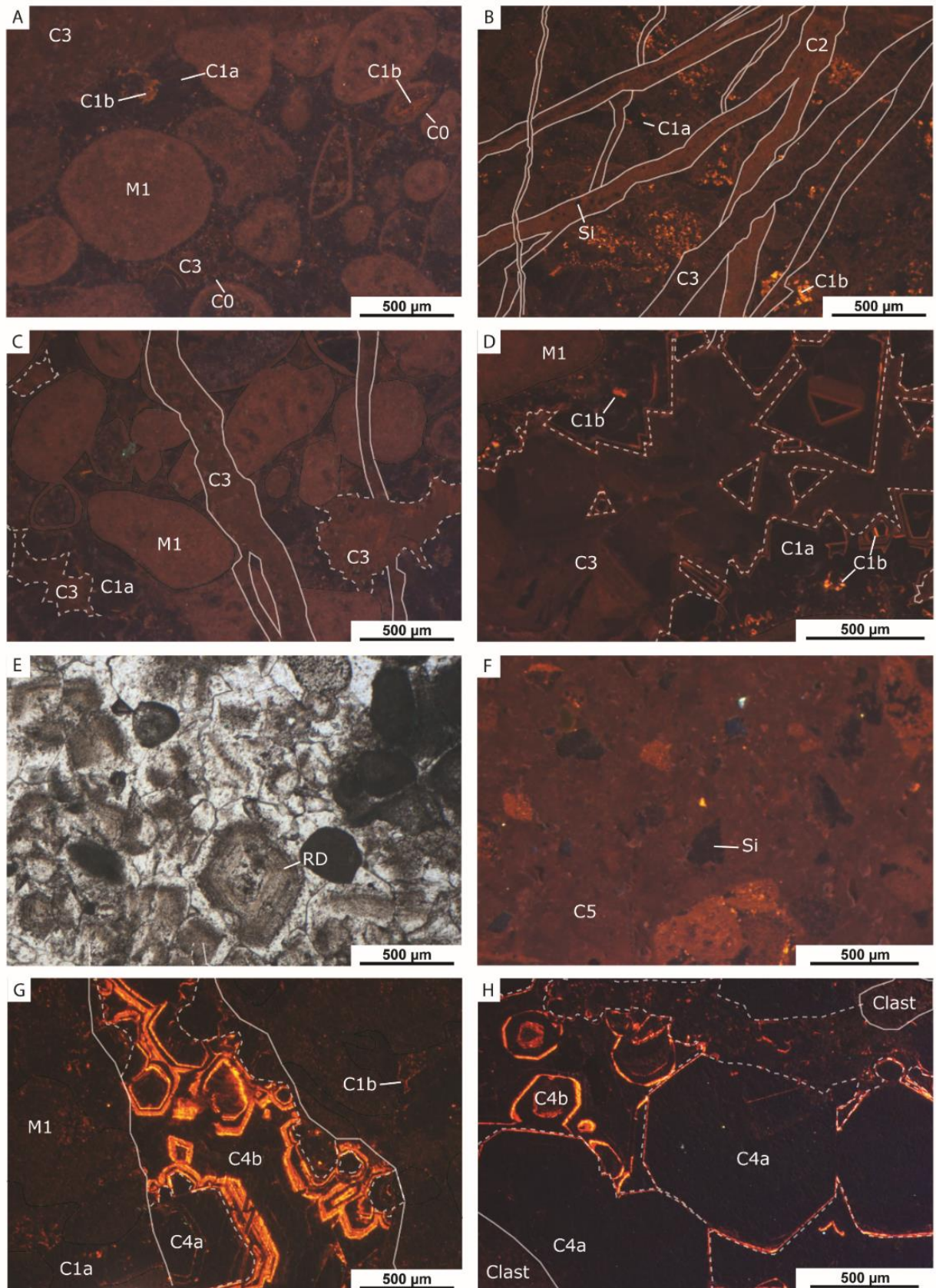


**Figure 5** : Thin-sections under cathodoluminescence; A: Calcarenite in transect 3 with micritised grain (M1), and intergranular volume cemented with C1 a and b and C3; B: C2 (with Si) and C3 veins affecting Castellans FR1 clasts with micritised grains cemented by C1b; C: C3 veins, cements and intergranular volumes in Castellans fault zone; D: C1 (a and b) and C3 cementing moldic porosity of transect 3 calcarenite; E: FR1 matrix with phantom of cloudy appearance replacive dolomite (RD); F: FR1 matrix de-dolomitized by C5 containing quartz grains; G: C4 (a and b) cementing vein of D19 fault zone; H: matrix of D19 FR2 cemented by C4 (a and b).

- 232 - C3 is a blocky calcite with non to red-dull luminescence in veins, moldic and  
233 intergranular pores (Fig. 5B, C, D). This cement also occurs in few veins of D19 sectors  
234 but is not restricted only to the fault zone.
- 235 - Phantoms of planar-e (euhedral) dolomite crystals (Sibley and Gregg, 1987) with a  
236 maximum size of 500  $\mu\text{m}$  affect the matrix of FR1 (Fig. 5E). They are vestiges of a  
237 previous dolomitization phase. They have a cloudy appearance caused by solid micritic  
238 inclusion inside crystals and can be considered as replacive dolomite (RD; Machel,  
239 2004). Within the FR1 matrix, an important concentration of angular grains of quartz  
240 with a maximum size of 300  $\mu\text{m}$  is noticed (Fig. 5F).
- 241 - A blocky calcite C4 (referred to as S2 in Aubert et al. (2019a)) is mainly present in veins  
242 of the D19 outcrop, in matrix of FRA, and intergranular and moldic pores (Fig. 5G, H).  
243 This cement shows zonation of non-luminescent and bright luminescent bands and can  
244 be divided in two sparitic sub-phases: C4a which is non-luminescent with some highly  
245 luminescent bands and C4b is bright luminescent with some thin non-luminescent  
246 zones. C4a occurs in lesser proportion in some veins along transect 2 and 3 of the  
247 Castellas fault.
- 248 - A sparitic cement C5, with a red-dull luminescence replaces the RD phase (Fig. 5F).

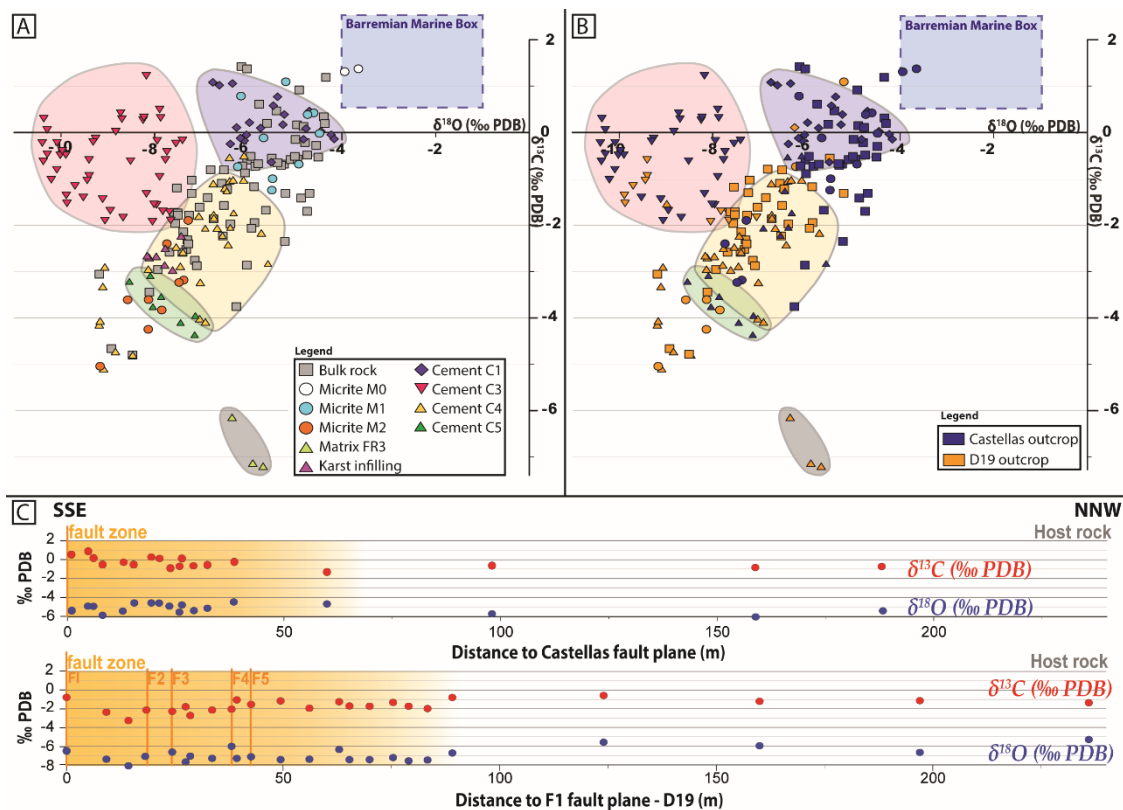
### 249 c. Additional diagenetic features

250 In addition to cementation phases, other diagenetic elements affected both fault zones. Karst  
251 infilling occurs in the F2 fault zone of the D19 outcrop. It is composed of well-sorted grains  
252 deposited in laminated layers. This karst deposit presents a stack of alternating micrite-rich and  
253 grain-rich layers from the latter composed of former blocky calcite belonging to dissolved  
254 grainstones. The laminated layers are affected by veins and stylolites; some of these are  
255 deformed due to the grain fall on sediments. Micritic layers have been observed under SEM,  
256 and the micrite appeared tight with compact subhedral mosaic crystals (Fig. 4F). We observed  
257 oxide filling mainly in the Castellas area in dissolution voids affecting C1a, C1b and C3  
258 cementation phases and in D19 in karstic fill. The areal amount of oxides increase close to  
259 stylolites.

## 260 3. CARBON AND OXYGEN ISOTOPES

261 Isotope measurements were realized on samples collected along transects of the fault zones. A  
262 hundred and eighty-nine measurements of C and O isotopes were performed on 16 samples and  
263 32 thin sections (Fig. 6A, table 2).

264 Sampling was done in bulk rock (66), sparitic cement (101; veins, intergranular volume and  
265 fault rock cements) and in fault rocks (10) in order to determine their isotopic signature. Isotopic  
266 values range from -10.40‰ to -3.65‰ for  $\delta^{18}\text{O}$  and from -7.20‰ to +1.42‰ for  $\delta^{13}\text{C}$  (Fig. 6A,  
267 B, table 2). The bulk rock values range from -9.18‰ to -4.34‰ for  $\delta^{18}\text{O}$  and from -4.80‰ to  
268 +1.19‰ for  $\delta^{13}\text{C}$  (Fig. 6A, table 2). These values are split in two sets. Set 1 includes transect  
269 transect 1 and 3 of the Castellas Fault. Bulk values range from -6.07‰ to -4.34‰ for  $\delta^{18}\text{O}$  and  
270 from -1.41‰ to +1.19‰ for  $\delta^{13}\text{C}$ . Set 2 includes transect 2 (Castellas) and transect 4 (D19).  
271 Bulk values range from -9.18‰ to -5.20‰ for  $\delta^{18}\text{O}$  and from -4.80‰ to -0.60‰ for  $\delta^{13}\text{C}$  (Fig.  
272 6B, table 2). In transect 3, the isotopic values only slightly vary, ranging from -6.13‰ to -  
273 4.50‰ for  $\delta^{18}\text{O}$  and from -1.41‰ to +0.47‰ for  $\delta^{13}\text{C}$  respectively (Fig. 6C, table 2). On the  
274 contrary, values are more variable along the D19 transect; they range from -9.18‰ to -5.20‰



276

277 **Figure 6** : Isotopic values of  $\delta^{13}\text{C}$  and  $\delta^{18}\text{O}$  measured on bulk rock, cement phases, and micrite. Range values of “Urgonian  
 278 marine box” from Moss & Tucker (1995) and Godet et al. (2006); A: set of values sorted by the nature of diagenetic phases  
 279 and B: values sorted by the fault zone; C: lateral evolution of  $\delta^{13}\text{C}$  and  $\delta^{18}\text{O}$  bulk isotopic values in Castellas (top) and in D19  
 280 (bottom) fault zones.

281 for  $\delta^{18}\text{O}$  and from  $-4.80\text{‰}$  to  $-0.60\text{‰}$  for  $\delta^{13}\text{C}$  (Fig. 6C, table 2). The  $\delta^{13}\text{C}$  values depletes  
 282 approaching to faults, especially south of F2.

283 Isotopic values of cements filling veins, intergranular volumes, karst infillings, and fault rocks  
 284 are divided into 5 groups (Fig. 6A, table 2):

- 285 - Isotopic values of C1 cement fluctuates from  $-6.76\text{‰}$  to  $-4.45\text{‰}$  for  $\delta^{18}\text{O}$  and from  $-$   
 286  $1.28$  to  $+1.08\text{‰}$  for  $\delta^{13}\text{C}$ ;
- 287 - Isotopic values of C3 cement ranges from  $-10.40\text{‰}$  to  $-6.73\text{‰}$  for  $\delta^{18}\text{O}$  and from  $-2.09$   
 288 to  $+1.22\text{‰}$  for  $\delta^{13}\text{C}$ ;
- 289 - Isotopic values of C4 cement in FR1 and FR2 matrix and in karst infillings ranges from  
 290  $-9.18\text{‰}$  to  $-4.60\text{‰}$  for  $\delta^{18}\text{O}$  and from  $-5.10\text{‰}$  to  $-0.74\text{‰}$  for  $\delta^{13}\text{C}$  with a positive  
 291 covariance between  $\delta^{18}\text{O}$  and  $\delta^{13}\text{C}$ . FR2 matrix values (from  $-6.55$  to  $-7.06\text{‰}$  for  $\delta^{18}\text{O}$   
 292 and from  $-1.10$  to  $-2.24\text{‰}$  for  $\delta^{13}\text{C}$ ) present slightly less depleted values than karst  
 293 infillings with mean values of  $-7.83\text{‰}$  and  $-2.53\text{‰}$  respectively for  $\delta^{18}\text{O}$  and  $\delta^{13}\text{C}$   
 294 respectively. (Fig. 6A). In the Castellas fault, 4 isotopic values from two veins are  
 295 enriched with means of  $-6.25$  and  $-4.2\text{‰}$  for  $\delta^{18}\text{O}$   $-0.64$  and  $-0.09\text{‰}$  for  $\delta^{13}\text{C}$  having  
 296 similar positive covariance than the other C4 values;
- 297 - Isotopic values of C5 cement, sampled in FR1 matrix display mean of  $-7.49\text{‰}$  for  $\delta^{18}\text{O}$   
 298 and  $-4.01\text{‰}$  for  $\delta^{13}\text{C}$  (Fig. 6A);

299 - Isotopic values of FR3 matrix with a mean of -5.98‰ for  $\delta^{18}\text{O}$  and -6.83‰ for  $\delta^{13}\text{C}$   
 300 (Fig. 6A)

301

302 **Table 2:** Carbon and oxygen isotope values of bulk carbonates for Castellás fault zone and D19  
 303 fault zones. *B:* bulk measurement; *M:* micrite value; *C1, C3, C4, C5:* cement isotopic value;  
 304 *FR:* fault rock isotopic value.

Transect	Sample	$\delta^{13}\text{C}$ (‰VPDB)	$\delta^{18}\text{O}$ (‰VPDB)	Class	Distance to F. (m)
Transect 1 (Cast.)	201	1,19	-4,34	B	1,3
Transect 1 (Cast.)	201	1,02	-6,62	C1	1,3
Transect 1 (Cast.)	201	1,31	-3,94	M	1,3
Transect 1 (Cast.)	201	1,37	-3,65	M	1,3
Transect 1 (Cast.)	213	-0,68	-5,24	B	22,7
Transect 1 (Cast.)	213	-0,58	-5,10	B	22,7
Transect 1 (Cast.)	213	-0,18	-6,09	C1	22,7
Transect 1 (Cast.)	213	0,03	-4,45	C1	22,7
Transect 1 (Cast.)	213	0,09	-4,77	C1	22,7
Transect 1 (Cast.)	213	-2,09	-6,92	C4	22,7
Transect 1 (Cast.)	213	-0,68	-4,92	M	22,7
Transect 2 (Cast.)	c3b17	-0,52	-5,95	B	4,6
Transect 2 (Cast.)	c3b17	-2,07	-6,38	C4	4,6
Transect 2 (Cast.)	c3b7	-0,64	-5,51	B	9,3
Transect 2 (Cast.)	c3b26	-3,76	-6,26	B	22,6
Transect 2 (Cast.)	c3b26	-2,85	-5,58	C4	22,6
Transect 2 (Cast.)	c3b26	-1,31	-4,69	B	57,3
Transect 2 (Cast.)	c3b7	-1,76	-6,31	C1	57,3
Transect 2 (Cast.)	c3b7	-1,28	-6,46	C1	57,3
Transect 2 (Cast.)	c3b26	-2,35	-5,22	M	57,3
Transect 2 (Cast.)	c3b26	-1,70	-4,75	M	57,3
Transect 3 (Cast.)	327	-0,24	-7,55	C3	0,3
Transect 3 (Cast.)	325	-1,90	-9,06	C3	0,3
Transect 3 (Cast.)	325	-1,69	-8,95	C3	0,3
Transect 3 (Cast.)	327	-3,11	-8,09	C4	0,3
Transect 3 (Cast.)	327	0,47	-5,40	B	1,0
Transect 3 (Cast.)	327	-0,18	-7,95	C3	1,0
Transect 3 (Cast.)	327	-0,17	-7,41	C3	1,0
Transect 3 (Cast.)	328	0,10	-5,74	C1	1,6
Transect 3 (Cast.)	328	-1,32	-8,18	C3	1,6
Transect 3 (Cast.)	328	-0,59	-7,77	C3	1,6
Transect 3 (Cast.)	328	-0,42	-7,74	C3	1,6
Transect 3 (Cast.)	328	-0,13	-9,26	C3	1,6
Transect 3 (Cast.)	328	0,02	-8,83	C3	1,6

Transect 3 (Cast.)	328	0,29	-8,70	C3	1,6
Transect 3 (Cast.)	328	0,42	-8,73	C3	1,6
Transect 3 (Cast.)	328	0,50	-7,89	C3	1,6
Transect 3 (Cast.)	328	1,22	-8,18	C3	1,6
Transect 3 (Cast.)	333	-1,84	-8,67	C3	1,6
Transect 3 (Cast.)	333	-0,96	-7,89	C3	1,6
Transect 3 (Cast.)	328	-0,14	-4,17	C4	1,6
Transect 3 (Cast.)	328	-0,05	-4,23	C4	1,6
Transect 3 (Cast.)	329	0,16	-4,95	B	2,4
Transect 3 (Cast.)	333	-0,25	-6,38	C1	4,6
Transect 3 (Cast.)	333	-0,12	-6,17	C1	4,6
Transect 3 (Cast.)	333	-0,62	-8,52	C3	4,6
Transect 3 (Cast.)	333	-0,12	-5,67	M	4,6
Transect 3 (Cast.)	333	-0,02	-4,48	M	4,6
Transect 3 (Cast.)	333	0,42	-4,60	M	4,6
Transect 3 (Cast.)	337	0,19	-5,59	B	9,5
Transect 3 (Cast.)	302	-0,53	-4,50	B	11,8
Transect 3 (Cast.)	302	-0,49	-4,74	B	11,8
Transect 3 (Cast.)	302	-0,62	-10,38	C3	11,8
Transect 3 (Cast.)	302	-0,49	-10,02	C3	11,8
Transect 3 (Cast.)	305	0,33	-4,38	B	16,0
Transect 3 (Cast.)	306	0,21	-4,35	B	17,8
Transect 3 (Cast.)	307	-0,01	-4,46	B	18,2
Transect 3 (Cast.)	308	-0,57	-4,95	B	20,0
Transect 3 (Cast.)	308	-1,44	-9,11	C3	20,0
Transect 3 (Cast.)	308	-0,23	-10,40	C3	20,0
Transect 3 (Cast.)	308	-0,22	-10,08	C3	20,0
Transect 3 (Cast.)	309	-1,41	-4,87	B	20,5
Transect 3 (Cast.)	309	-0,52	-5,01	B	20,5
Transect 3 (Cast.)	309	-0,15	-4,82	C1	20,5
Transect 3 (Cast.)	309	-1,56	-7,96	C3	20,5
Transect 3 (Cast.)	309	-1,55	-8,01	C3	20,5
Transect 3 (Cast.)	312	0,12	-4,81	B	23,2
Transect 3 (Cast.)	314	-0,71	-5,30	B	25,9
Transect 3 (Cast.)	314	-0,80	-10,09	C3	25,9
Transect 3 (Cast.)	314	-0,49	-9,90	C3	25,9
Transect 3 (Cast.)	314	-0,47	-10,29	C3	25,9
Transect 3 (Cast.)	314	-0,40	-9,97	C3	25,9
Transect 3 (Cast.)	314	0,06	-10,30	C3	25,9
Transect 3 (Cast.)	316	-1,24	-5,50	B	29,2
Transect 3 (Cast.)	316	-1,00	-5,48	B	29,2
Transect 3 (Cast.)	316	-0,22	-4,79	B	29,2
Transect 3 (Cast.)	316	-1,02	-10,21	C3	29,2
Transect 3 (Cast.)	316	-0,18	-9,31	C3	29,2
Transect 3 (Cast.)	316	0,30	-10,37	C3	29,2
Transect 3 (Cast.)	318	-0,28	-4,53	B	35,4

Transect 3 (Cast.)	320	-0,68	-5,79	B	96,1
Transect 3 (Cast.)	322	-0,88	-6,07	B	158,0
Transect 3 (Cast.)	323	-0,65	-5,37	B	188,0
Castellas (ZF1)	Z1,1	0,17	-5,26	C1	0,0
Castellas (ZF1)	Z1,1	0,39	-5,23	C1	0,0
Castellas (ZF1)	Z1,1	0,46	-4,70	C1	0,0
Castellas (ZF1)	Z1,2	0,21	-5,98	C1	0,0
Castellas (ZF1)	Z1,1	-0,55	-6,40	C4	0,0
Castellas (ZF1)	Z1,1	-0,52	-6,10	C4	0,0
Castellas (ZF1)	Z1,2	-4,12	-7,45	C5	0,0
Castellas (ZF1)	Z1,2	-0,15	-4,99	FR	0,0
Castellas (ZF1)	Z1,2	0,39	-4,73	M	0,0
Castellas (ZF1)	Z1,2	0,61	-5,77	M	0,0
Castellas (ZF1)	Z1,1	0,78	-6,16	M	0,0
Castellas (ZF2)	Z2,2	0,77	-5,38	C1	0,0
Castellas (ZF2)	Z2,7	-1,40	-9,52	C3	0,0
Castellas (ZF2)	Z2,7	-4,38	-7,15	C5	0,0
Castellas (ZF2)	Z2,7	-3,97	-7,13	C5	0,0
Castellas (ZF2)	Z2,7	-3,78	-8,04	C5	0,0
Castellas (ZF2)	Z2,7	-3,56	-7,86	C5	0,0
Castellas (ZF2)	Z2,7	-3,24	-7,48	C5	0,0
Castellas (ZF2)	Z2,7	-3,23	-8,54	C5	0,0
Castellas (ZF2)	Z2,2	0,58	-5,47	FR	0,0
Castellas (ZF2)	Z2,2	0,92	-4,91	FR	0,0
Castellas (ZF2)	Z2,7	-1,68	-5,63	FR	0,0
Castellas (ZF2)	Z2,7	-2,24	-6,55	FR	0,0
Castellas (ZF2)	Z2,7	-3,18	-7,38	M	0,0
Castellas (ZF2)	Z2,7	-2,86	-6,03	FR	1,0
Castellas (ZF5)	Z5,4	0,27	-8,25	C3	0,0
Castellas (ZF5)	Z5,4	0,31	-7,87	C3	0,0
Castellas (ZF5)	Z5,4	0,32	-8,23	C3	0,0
Castellas (ZF5)	Z5,4	1,06	-6,34	C1	0,4
Castellas (ZF5)	Z5,4	1,08	-6,76	C1	0,4
Castellas (ZF5)	Z5,4	1,05	-7,13	FR	0,4
Castellas (ZF5)	Z5,4	1,37	-6,03	FR	0,4
Castellas (ZF5)	Z5,4	1,42	-6,15	FR	0,4
Transect	Sample	$\delta^{13}\text{C}$ (‰VPDB)	$\delta^{18}\text{O}$ (‰VPDB)	Class	Distance to F1 (m)
Transect 4 (D19)	3B	-0,81	-6,52	B	0,0
Transect 4 (D19)	3B	-1,20	-6,50	C1	0,0
Transect 4 (D19)	3B	-1,02	-6,33	C1	0,0
Transect 4 (D19)	3B	0,11	-6,25	C1	0,0
Transect 4 (D19)	3B	-0,74	-6,23	M	0,0
Transect 4 (D19)	9	-2,32	-7,30	B	9,2

Transect 4 (D19)	13a	-3,44	-8,11	B	14,3
Transect 4 (D19)	13a	-2,96	-7,93	B	14,3
Transect 4 (D19)	13C	-2,97	-7,62	M	14,3
Transect 4 (D19)	13C	-2,86	-7,79	M	14,3
Transect 4 (D19)	13C	-2,70	-8,12	M	14,3
Transect 4 (D19)	13C	-2,67	-7,96	M	14,3
Transect 4 (D19)	13C	-2,66	-8,16	M	14,3
Transect 4 (D19)	13C	-2,50	-7,77	M	14,3
Transect 4 (D19)	13C	-1,54	-8,98	M	14,3
Transect 4 (D19)	17	-2,58	-7,68	B	18,7
Transect 4 (D19)	14A	-1,97	-6,38	B	18,7
Transect 4 (D19)	14A	-1,87	-6,74	B	18,7
Transect 4 (D19)	15B	-2,23	-7,43	B	18,7
Transect 4 (D19)	17	-1,05	-6,40	C1	18,7
Transect 4 (D19)	14A	-1,77	-6,74	C1	18,7
Transect 4 (D19)	14A	-2,42	-6,43	C4	18,7
Transect 4 (D19)	14A	-2,06	-6,67	C4	18,7
Transect 4 (D19)	21	-2,23	-6,54	B	24,4
Transect 4 (D19)	RSG	-1,90	-7,66	B	28,4
Transect 4 (D19)	RSG	-1,70	-7,83	B	28,4
Transect 4 (D19)	RSD	-2,87	-7,10	B	29,5
Transect 4 (D19)	RSD	-2,76	-7,14	B	29,5
Transect 4 (D19)	RSD	-0,93	-9,40	C3	29,5
Transect 4 (D19)	RSF1	-2,40	-7,28	B	34,7
Transect 4 (D19)	RSF2	-2,14	-7,39	B	34,7
Transect 4 (D19)	RSF2	-1,78	-7,27	B	34,7
Transect 4 (D19)	RSF1	-1,03	-9,44	C3	34,7
Transect 4 (D19)	RSF2	-1,93	-8,05	C3	34,7
Transect 4 (D19)	RSF2	-0,59	-9,40	C3	34,7
Transect 4 (D19)	RSF2	-2,95	-8,14	C4	34,7
Transect 4 (D19)	RSE 1	-2,53	-7,33	B	35,0
Transect 4 (D19)	RSE 2	-2,59	-7,41	B	35,0
Transect 4 (D19)	RSE 1	-1,71	-7,68	C3	35,0
Transect 4 (D19)	RSE 2	-1,84	-6,73	C3	35,0
Transect 4 (D19)	57	-2,07	-5,93	B	38,1
Transect 4 (D19)	57	-1,94	-5,87	B	38,1
Transect 4 (D19)	57	-1,83	-7,06	C3	38,1
Transect 4 (D19)	57	-1,10	-6,75	C3	38,1
Transect 4 (D19)	57	-4,02	-7,04	C4	38,1
Transect 4 (D19)	57	-2,17	-5,72	C4	38,1
Transect 4 (D19)	57	-1,58	-6,52	FR	38,1
Transect 4 (D19)	57	-7,20	-5,68	M	38,1
Transect 4 (D19)	57	-7,13	-5,90	M	38,1
Transect 4 (D19)	28b	-1,03	-7,21	B	39,3
Transect 4 (D19)	28b	-1,03	-6,10	C3	39,3
Transect 4 (D19)	28b	-4,09	-6,92	C4	39,3

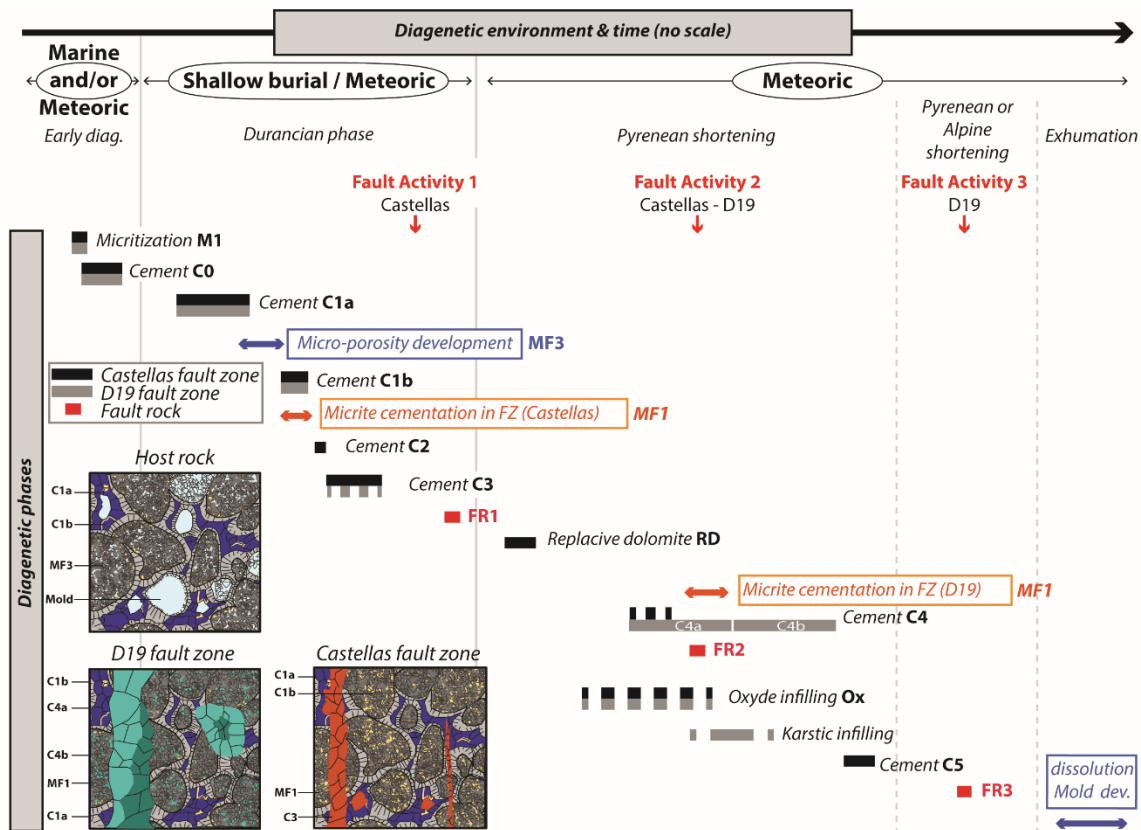


Transect 4 (D19)	28b	-2,58	-7,40	C4	39,3
Transect 4 (D19)	28b	-2,47	-7,54	C4	39,3
Transect 4 (D19)	30a	-1,61	-7,04	B	42,6
Transect 4 (D19)	30a	-1,41	-6,87	B	42,6
Transect 4 (D19)	30a	-3,23	-7,03	C4	42,6
Transect 4 (D19)	30a	-2,89	-7,45	C4	42,6
Transect 4 (D19)	24a	-1,21	-7,52	B	51,1
Transect 4 (D19)	27b	-1,92	-7,48	B	57,9
Transect 4 (D19)	31	-1,24	-6,44	B	65,0
Transect 4 (D19)	32	-1,75	-7,50	B	67,4
Transect 4 (D19)	34	-1,79	-7,49	B	72,2
Transect 4 (D19)	36	-1,32	-7,21	B	77,8
Transect 4 (D19)	38	-1,73	-7,59	B	81,5
Transect 4 (D19)	62	-1,96	-7,56	B	86,0
Transect 4 (D19)	42	-0,81	-6,80	B	91,9
Transect 4 (D19)	63	-0,55	-5,50	B	124,0
Transect 4 (D19)	64	-1,17	-5,88	B	160,0
Transect 4 (D19)	65	-1,10	-6,57	B	197,0
Transect 4 (D19)	66	-1,31	-5,21	B	236,0
Transect 4 (D19)	60a	-3,06	-9,18	B	255,2
Transect 4 (D19)	60B	-4,80	-8,47	B	255,2
Transect 4 (D19)	60B	-4,66	-8,92	B	255,2
Transect 4 (D19)	61	-1,53	-9,87	C3	255,2
Transect 4 (D19)	61	-1,36	-9,89	C3	255,2
Transect 4 (D19)	60a	-1,15	-9,70	C3	255,2
Transect 4 (D19)	60a	-3,32	-9,11	C4	255,2
Transect 4 (D19)	60B	-5,10	-9,09	C4	255,2
Transect 4 (D19)	60B	-4,73	-8,84	C4	255,2
Transect 4 (D19)	60B	-4,15	-9,18	C4	255,2
Transect 4 (D19)	60B	-4,07	-9,16	C4	255,2
Transect 4 (D19)	60B	-2,90	-9,06	C4	255,2
Transect 4 (D19)	60a	-3,83	-7,85	M	255,2
Transect 4 (D19)	60B	-5,04	-9,17	M	255,2
Transect 4 (D19)	60B	-4,25	-8,14	M	255,2
Transect 4 (D19)	60B	-3,61	-8,58	M	255,2
Transect 4 (D19)	60B	-3,61	-8,13	M	255,2

## 305 6. DISCUSSION

### 306 1. DIAGENETIC EVOLUTION OF THE FAULT ZONES

307 The chronological relations between cements can be established via to cross-cutting relations  
308 and inclusion principles. Indeed, the veins filled with cement C2 cross-cut C1a and C1b cements  
309 (Fig. 5B). Thus, C2 cementation post-dated C1 cement. C3 veins cross-cut the C2 veins, but  
310 are included within FR1 clasts (Fig. 5B). Hence, C3 cement is prior to FR1 development but  
311 after C2 cementation. The fault rock 1 (FR1) is related to the first extensional fault activity,  
312 consequently, C1, C2 and C3 cementation phases occurred prior to the proper fault plane and



313

314 **Figure 7:** Paragenetic sequence of the both fault zones (black: Castellás, grey: D19) with micro-porosity development  
 315 (blue), cementation (orange) and fault zone activation events (red).

316 fault core formation and are related to the fault nucleation. Replacive dolomite is found within  
 317 FR1 matrix (Fig. 5E), therefore, it developed after FR1 formation. Finally, the C4 cement can  
 318 be noticed within FR2 matrix indicating that C4 cementation event post-dated FR2 formation.  
 319 The fault rock 2 (FR2) developed during strike-slip reactivation of the studied faults. The  
 320 combined superposition, overlap, cross-cutting principles and isotopic signature of cements  
 321 brought out the chronology between phases, and revealed the paragenetic sequence (Fig. 7).

322 The Urgonian carbonates in La Fare anticline underwent 3 major diagenetic events, which  
 323 impacted the host rock and/or the fault zones. We discriminate among diagenetic events that  
 324 occurred before and during faulting.

### 325 a. Pre fault diagenesis – microporosity development

326 During Upper Barremian, just after deposition, micro-bores organisms at the sediment-water  
 327 interface enhanced the formation of micritic calcitic envelopes on bioclasts, ooids and peloids  
 328 (Purser, 1980; Reid and Macintyre, 2000; Samankassou et al., 2005; Vincent et al., 2007). This  
 329 micritisation in marine conditions is typical for Urgonian low-energy inner platform  
 330 environment (Fournier et al., 2011; Masse, 1976). Subsequently, C0 cement formed around  
 331 grains giving rise to a solid envelop inducing the preservation of the original grain shape during  
 332 the later burial compaction (Step 0 on Fig. 8). However, the majority of isotopic values do not  
 333 fit in the Barremian sea water calcite box which ranges from -1.00‰ to -4.00‰ for  $\delta^{18}\text{O}$  and  
 334 from +1.00‰ to +3.00‰ for  $\delta^{13}\text{C}$  (Fouke et al., 1996; Godet et al., 2006). Only two data points  
 335 pertaining to micritised grains show isotopic values close the Barremian sea water calcite. The  
 336 isotopic depletion of other data indicates the slight impact of C0 cementation on isotopic values.

337 The next sub-phase of cementation C1a partly fills intergranular porosity. This non luminescent  
338 cement with isotopic values ranging from -6.8‰ to -3.9‰ for  $\delta^{18}\text{O}$  and from -1.0‰ to +1.3‰  
339 for  $\delta^{13}\text{C}$  is characteristic of mixed fluids. Léonide et al. (2014) measured a calcite cement S1,  
340 near La Fare anticline with similar luminescence and isotopic range values (mean:  $\delta^{18}\text{O} =$   
341  $-5.49\text{‰}$ ;  $\delta^{13}\text{C} = +2.34\text{‰}$ ). These authors linked this cementation phase to a shallow burial  
342 meteoric fluid circulation under equatorial climate during Durancian uplift. This diagenetic  
343 event led to micrite re-crystallization, and to the development of microporosity (MF3). Since  
344 La Fare carbonates were exhumed at that time (Léonide et al., 2014) the meteoric fluids led to  
345 similar diagenetic modifications (Step 1 on Fig. 8):

- 346 (i) Micrite re-crystallization and microporosity MF3 setup by Ostwald ripening  
347 processes (Fig. 9B1a; Ostwald, 1886; Volery et al., 2010).
- 348 (ii) Cementation of C1a, partly filling intergranular porosity (Fig. 9B1b)

349 The micrite re-crystallization strongly increased rock porosity due to enhanced microporosity  
350 (Fig. 9B1a). Resulting from this event, Urganian carbonates formed a type III reservoir *sensu*  
351 Nelson (2001).

## 352 b. Fault-related diagenesis – alteration of reservoir properties

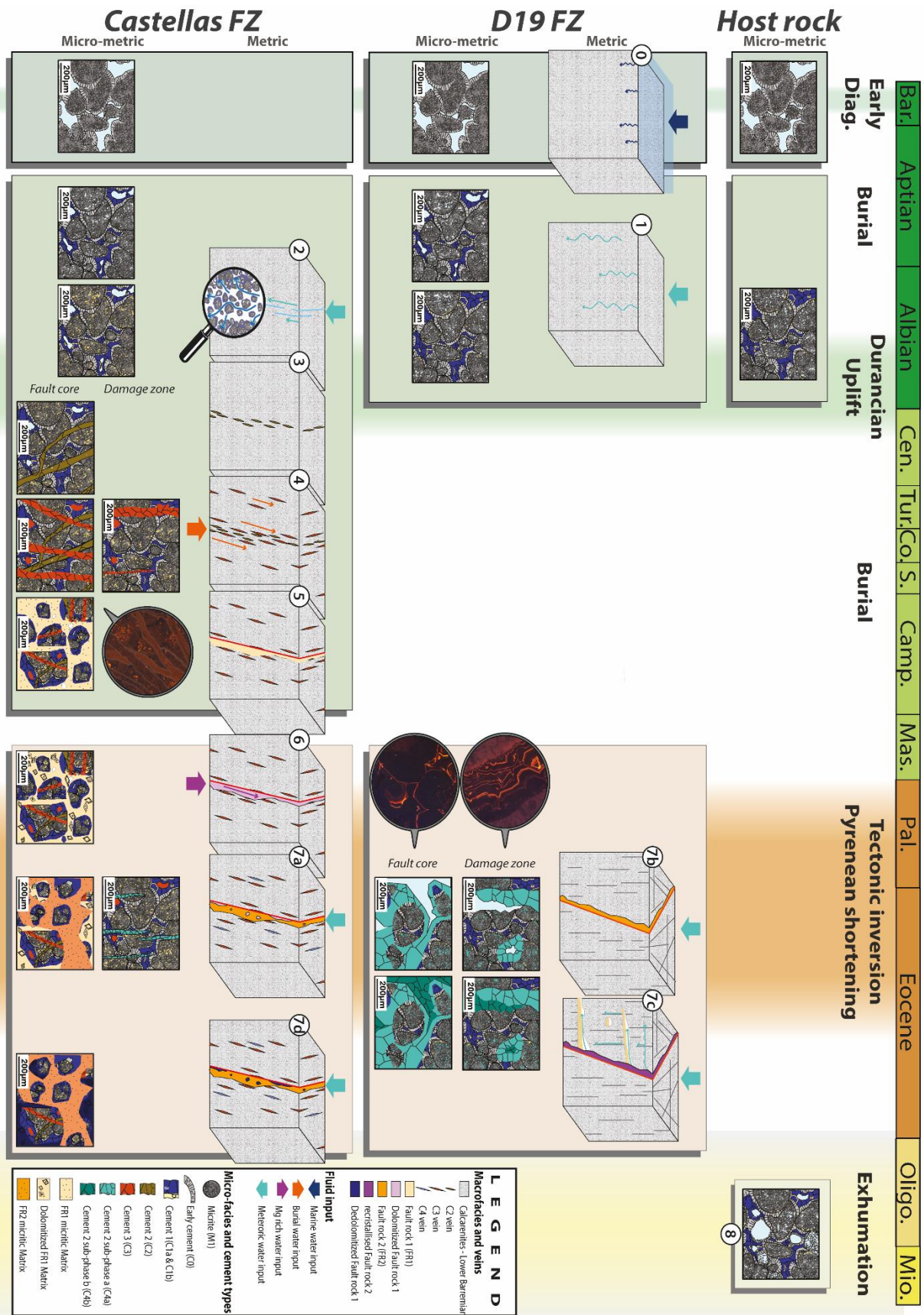
353

### 354 Normal faulting-related diagenesis

355 The Castellás fault first nucleated during Durancian uplift (Aubert et al., 2019b; Matonti et al.,  
356 2012) affecting the host Urganian carbonates.

357 In porous granular media, fault nucleation mechanisms can lead to dilation processes (Fossen  
358 and Bale, 2007; Fossen and Rotevatn, 2016; Main et al., 2000; Wilkins et al., 2007; Zhu and  
359 Wong, 1997) under low-confining pressure (<100 KPa; Alikarami and Torabi 2015). Because  
360 this process leads to dilatancy, it increases the rock permeability (Alikarami and Torabi, 2015;  
361 Bernard et al., 2002) in the first stage of deformation bands (Heiland et al., 2001; Lothe et al.,  
362 2002) enhancing fluid flows.

363 Castellás fault zone nucleated within a partially and dimly cemented host rock under low-  
364 confining pressure, in an extensional stress regime, at a depth <1 km (Lamarche et al. 2012).  
365 Under these conditions, Barremian host rock were likely characterised by mechanical and  
366 petrographical properties close to porous granular media described above. Moreover, Micarelli  
367 et al. (2006) showed that, during early stages of deformation, fault zones in carbonates have a  
368 hydraulic behaviour comparable to deformation bands in carbonates. Hence, in the Urganian  
369 carbonates of La Fare area, dilatant processes occurred as an incipient fault mechanism and  
370 enhanced fluid circulations along the deformation bands. Fluid flows led to the cementation of  
371 C1b (Step 2 on Fig. 8). However, dilation bands were likely unstable and grain collapse occurred  
372 swiftly after the beginning of the deformation due to an increase in the loading stress (Lothe et  
373 al., 2002). This could be the explanation why C1b does not fill all intergranular porosity.  
374 Consequently, as all micritic grains in fault zone are cemented by C1b, the bulk isotopic  
375 measurements are strongly influenced by C1 cement isotopic values. This is the explanation  
376 why in transect 3 the bulk isotopic values 30 m apart from the fault (means of -5.26‰ for  $\delta^{18}\text{O}$   
377 and -0.82‰ for  $\delta^{13}\text{C}$ ) are close to bulk isotopic values far from the fault plane (188 m; -5.37‰  
378 for  $\delta^{18}\text{O}$  and -0.65‰ for  $\delta^{13}\text{C}$ , Fig. 6A). Dilation bands have also been described by Kaminskaite  
379 et al. (2019) in the San Vito Lo Capo carbonates grainstones (Sicily, Italy). These dilation bands  
380 also led to selective cementation of the carbonate rocks and to a microporosity decrease.

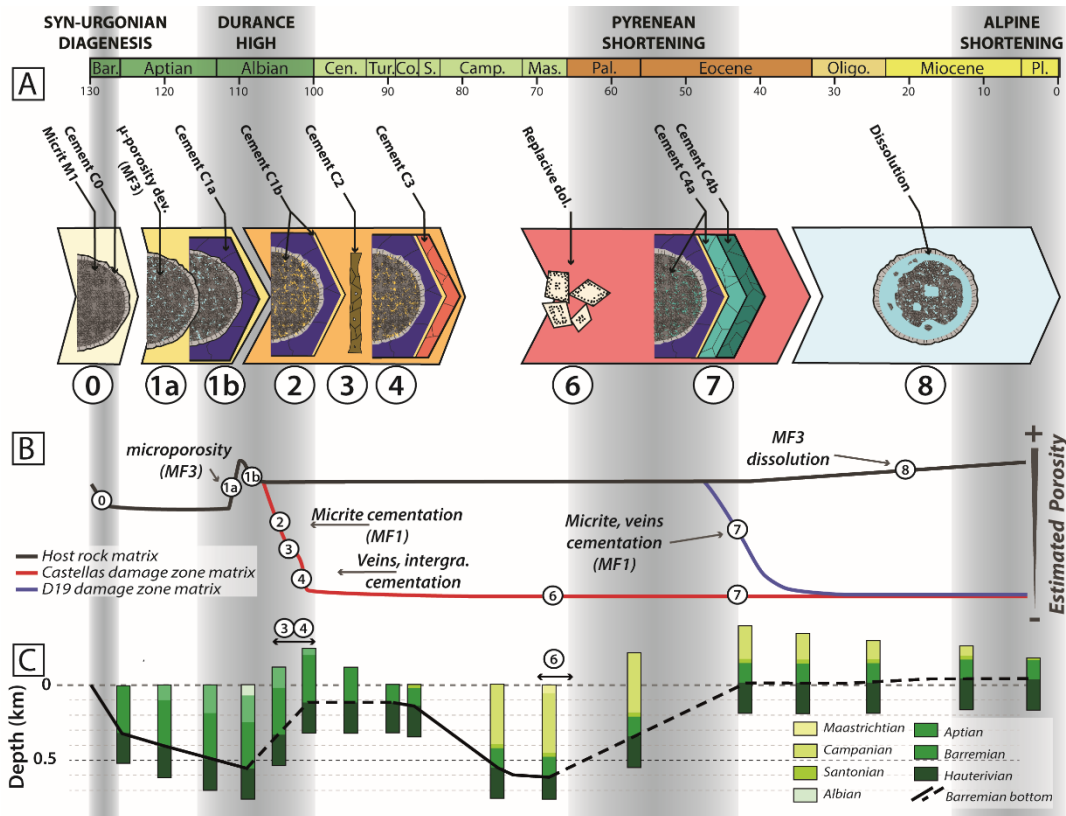


381

382

383

**Figure 8 :** Diagenetic and geodynamic evolution since the Barremian of both fault zones and host rock at the metric and micro-metric scale. Numbers 0 to 8 correspond to the steps 0 to 8 (see text for description).



385

386 **Figure 9** : Evolution of reservoir properties. A: different cementation phases; numbers 0 to 8 correspond to the steps 0 to  
 387 8 (see text for description), B: relative porosity evolution of the host rock and the two fault zones; C: Burial/Uplift curve of  
 388 Barremian basement (modified from Matonti et al. (2012)).

389 Cementation (C1a and C1b) conferred a stiffer response of limestone to deformation, making  
 390 it prone to deform through brittle structures (joints and veins), rather than via granular  
 391 particulate flow (deformation bands).. During the first stages of fault evolution in low-porosity  
 392 limestones, intense fracturing of the fault zone predating fault core formation is known to  
 393 increase fault permeability (Micarelli et al., 2006). In the studied faults, the first brittle event  
 394 allowed Al-rich fluids to flow with fine-grained quartz grains in the incipient open fractures  
 395 leading to precipitation of C2 cement (Step 3 on Fig. 8). The Urgonian facies of the studied area  
 396 are composed of pure carbonates without siliciclastic input. Quartz grains and Aluminium could  
 397 have been reworked from surrounding formations. The rocks underlying the studied exposed  
 398 Urgonian carbonates are limestones and dolostones. Albian and Aptian rocks are marly and  
 399 sandy limestones, respectively (Anglada et al., 1977). Hence, Aptian layers are very likely to  
 400 be the source of quartz. The fluids may have carried small grains of quartz from the Aptian  
 401 sandy limestones via the fracture network. The Al enrichment of C2 could result from the  
 402 erosion of Albian and Aptian deposits during the Durancian uplift (Guendon and Parron, 1985;  
 403 Triat, 1982).

404 As the fault zone grew, new fracture sets formed, leading to new phase of calcite cementation  
 405 (C3) in veins and intergranular porosity (Step 4 on Fig. 8). The  $\delta^{18}\text{O}$  isotopic values of C3 range  
 406 from -10.40‰ to -6.73‰ with  $\delta^{13}\text{C}$  values between -2.09‰ and +1.22‰. As C3 cementation  
 407 occurred during the Durancian uplift and denudation, C3 most probably did not cement in deep  
 408 burial conditions (maximum depth of 500 m; Fig. 9C4).The negative  $\delta^{13}\text{C}$  values tend  
 409 corroborate the hypothesis of cementation induced by meteoric fluid rather than marine ones.  
 410 Hence, C3 would correspond to a shallow burial/meteoric cementation phase. Due to this

411 cementation, rocks in this zone tightened with porosity down to <5%. The porosity did not  
412 change since this event (Fig. 9B5). This porosity reduction due to cementation has also been  
413 observed in other cases of brittle-dilatant faults (Agosta et al., 2007; Celico et al., 2006;  
414 Gaviglio et al., 2009; Mozley and Goodwin, 1995). Following this, the fault zone was a barrier  
415 to fluid flow, leading to a reservoir compartmentalization. Fluids responsible for precipitation  
416 of C3 cement also occurred along fracture clusters of the D19 sector and led to vein formation.

417 In a later stage, the fault core formed and the fault plane *sensu-stricto* developed, leading to  
418 FR1 breccia with a permeable matrix with quartz grains >100 µm in size (Step 5 on Fig. 8).  
419 These grains either came from silica found inside C2 cement described above or from Aptian  
420 overlying rocks. Silica crystals in C2 veins are scarce and smaller than 10 µm. Thus, quartz  
421 grains may rather come from Aptian rocks like the ones found in C2 veins. The presence of  
422 Aptian quartz in the fault core proves that the Castellás fault affected also Aptian rocks, which  
423 were later eroded during the Durancian uplift. According to this, the fault activity occurred  
424 before total erosion of Aptian rocks. Un-cemented breccias within the fault core formed good  
425 fluid pathways (Billi et al., 2008; Delle Piane et al., 2016). In the studied fault, formation of  
426 FR1 breccia allowed the fault core to act as a drain. However, the cemented surrounding host  
427 rocks constrained the lateral extent of the drainage area of this high-permeable conduit. Un-  
428 cemented breccias acting as good across- and along- fluid pathways were also described on  
429 Apennines carbonate formations within fault cores of strike and extensional faults (Billi et al.,  
430 2003, 2008; Storti et al., 2003).

#### 431 **Tectonic Inversion – Castellás fault-related dolomitization**

432 At the onset of the Pyrenean shortening, compressive stresses led to underground water  
433 upwelling through the permeable fault core. This fluid flow triggered the dolomitization of FR1  
434 matrix (Step 6 on Fig. 8). This matrix-selective dolomitization could have been favoured by  
435 several factors:

- 436 (i) The matrix has higher permeability than cemented clasts with a smaller grain size,  
437 hence a higher grain surface area (Machel, 2004);
- 438 (ii) This type of upwelling fluids, so-called “squeegee-type”, are short lived processes  
439 (Buschkuehle and Machel, 2002; Deming et al., 1990; Dorobek, 1989; Machel et  
440 al., 2000) not favourable for massive dolomitization;
- 441 (iii) Low-temperature fluids, under 50°-80°C, enabled the preservation of FR1 clast  
442 initial structure. Contrarily, high-temperature dolomitization tends to be destructive  
443 (Machel, 2004);
- 444 (iv) The tight surrounding host rock constrained Mg-rich fluid circulation to the fault  
445 core domain.

446 Gisquet et al. (2013) noticed similar fault related replacive dolomitization phase in the Etoile  
447 massif, 23 km South-Est of the studied zones. They linked the dolomitization to contractional  
448 stress regime during the early (Late Cretaceous) Pyrenean shortening. According to these  
449 authors, the tectonic stress led to low-temperature upwelling fluids likely Mg-enriched by the  
450 dissolution of underlying Jurassic dolomites. The Jurassic dolomites also occur in La Fare  
451 anticline. Since the fluids leading to dolomitization of fault core were low-temperature and  
452 since dolomites occur underground, it is possible that the dolomitization in La Fare and in the  
453 Etoile massif was similar and synchronous. Matrix dolomitization can increase inter-crystalline

454 and/or inter-particle porosity up to 13% but the later dolomite overgrowth reduces the porosity  
455 and permeability (Lucia, 2004; Machel, 2004; Saller and Henderson, 2001). Hence, in the first  
456 stages of dolomitization, the fault core was an important drain. After the growth of dolomite  
457 crystals, the fault core turned into barrier (Fig. 9 B6 and C6)

#### 458 **Sinistral tectonic inversion – meteoric alteration of reservoir properties**

459 The ongoing tectonic inversion with increasing compressive stresses eventually led to the  
460 Castellás fault sinistral reactivation and to the onset of D19 fault zone (Aubert et al., 2019b).  
461 Aubert et al. (2019a) has shown that this compression reactivated the pre-existing early N030°  
462 background fractures (Step 7 on Fig. 8). This tectonic event formed FR2 in fault cores but with  
463 specific diagenetic consequences. In the D19 fault zone, the fault nucleation and reactivation of  
464 background fractures led to pluri-metric to kilometric fault surfaces with a permeable fault rock  
465 acting as drains and localizing the fluid flow (Aubert et al., 2019a). This fluid flow witnessed  
466 by the cementation of C4a and C4b in veins and micritised grains (MF1, Step 7c on Fig. 8),  
467 leading to a strong porosity decrease in the fault zone (Fig. 9,B7 and C7). However, not all  
468 fractures were cemented by C4, so that fracture porosity/permeability was still partially  
469 preserved. Therefore, the D19 fault zone became a type I reservoir *sensu* Nelson (2001) with a  
470 very low matrix porosity/permeability and high fracture-related secondary permeability (Aubert  
471 et al., 2019a).

472 Along F2, successive fluids gave rise to karsts, karstic infilling and dissolution/cementation  
473 processes of FR2 matrix (Step 7c on Fig. 8). Then, FR2 was sealed by C4 cementation. Isotopic  
474 values of C4 cement (from -9.2 to -6.1‰ for  $\delta^{18}\text{O}$  and from -5.01‰ to -1.0‰ for  $\delta^{13}\text{C}$ ) highlight  
475 the strong influence of meteoric fluids. This is coherent with the occurrence of karstic infilling  
476 due to fluid circulations in vadose zone, with alternating dissolution and cementation (Swart,  
477 2015). However, the positive covariance between  $\delta^{18}\text{O}$  and  $\delta^{13}\text{C}$  of C4 suggests mixed fluids  
478 (Allan and Matthews, 1982) of meteoric water and burial or marine water.

479 In the Castellás fault zone, the host rocks are slightly impacted by these meteoric fluid  
480 circulations. Yet, some veins filled with C4a cement occur along transect 2 and transect 3 (Step  
481 7a on Fig. 8). Two samples have enriched  $\delta^{18}\text{O}$  and  $\delta^{13}\text{C}$  isotopic values (respective means of -  
482 6.25‰ and -4.20‰ for  $\delta^{18}\text{O}$ ; -0.64 and -0.09‰ for  $\delta^{13}\text{C}$ ) similar to C1 cement (Fig. 6A). This  
483 indicates that C4 cement in the Castellás fault zone was precocious in comparison to the D19.  
484 C4 cement in Castellás area is restricted to transect 2. Transect 2 cross-cuts the Castellás fault  
485 along a relay zone (Fig. 2A). Relay or linkage zones occur where two fault segments overlap  
486 each other during fault grow (Kim et al., 2004; Long and Imber, 2011; Walsh et al., 1999, 2003).  
487 Consequently, the fault complexity, the fracture intensity and the fracture-strike range are  
488 increased (Kim et al., 2004; Sibson, 1996). This process in the studied area resulted in a well-  
489 connected fracture network that increased the permeability and favoured local fluid circulations.  
490 In transect 2, the increase of the local permeability in the relay zone enhanced fluid flow related  
491 to C4 cement. The relay zones along the Castellás fault and their consequences on the fracture  
492 permeability are, therefore, responsible for this local cementation event. On the contrary,  
493 cementation in D19 fault zone is linked to the highly permeable fault surfaces which acted as  
494 drains (Aubert et al., 2019a). This implies that the cementation occurred only after the  
495 development of the fault surface. In the case of Castellás, the relay zone was already present,  
496 inherited from the former extensional activity, allowing early C4 fluid to flow through the fault  
497 zone. This, in addition, explains why the early C4 cementation has not been recorded in D19

498 fault zone. The C4 cementation in transect 2 reduced the porosity to less than 8% on a larger  
499 zone (>60 m) than in both others transects (transect 1 ≈30m, transect 3>40m).

500 The reactivation of the Castellás fault formed a new fracture network that locally triggered the  
501 fracture connectivity and permeability. The Castellás fault zone formed a type I reservoir  
502 (Nelson, 2001), but lateral variation of the fracture network implies lateral variations of the  
503 hydraulic properties. Thus, the fault zone was both a drain and a barrier (Matonti et al., 2012).  
504 In this case, the most appropriate concept would be a sieve, because in this analogy, it is  
505 synchronously closed in places and open in other places.

506 After these events, the matrix of the Castellás fault core was de-dolomitized (FR1) in relation  
507 to cementation C5 (Step 7d on Fig. 8). The C5 cement isotope values (mean of -7.49‰ for  $\delta^{18}\text{O}$   
508 and -4.01‰ for  $\delta^{13}\text{C}$ ) are comprised within C4 positive covariance between  $\delta^{18}\text{O}$  and  $\delta^{13}\text{C}$ . This  
509 indicates a continuity between C4 and C5 fluid flows. The measurements with the SEM  
510 revealed a lack of Mg in the matrix indicating that C5 totally recrystallised the replacive  
511 dolomite. Following this de-dolomitization phase, no additional diagenetic event is recorded in  
512 Castellás fault zone.

513 A late Pyrenean to Alpine compression reactivated the D19 fault zone what formed the new  
514 fault rock FR3. The matrix of this fault rock has very low  $\delta^{13}\text{C}$  isotopic values (mean of -6.83‰)  
515 indicating an organic matter input (Swart, 2015). This implies fluids percolating soils, as results  
516 from a near surface fluid circulation. We deduce that the D19 faults was lately reactivated after  
517 the folding of the La Fare anticline. There is no such cementation with similar isotope values  
518 in the fault zone, meaning that fluids and cements did not alter the fault zone diagenetic  
519 properties.

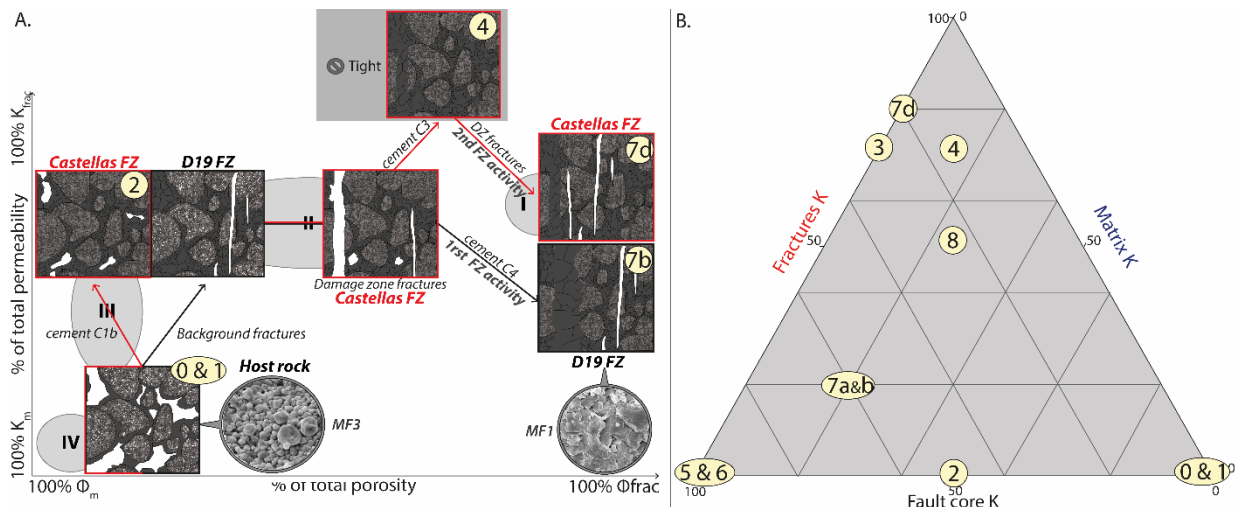
520 Eventually, the late exhumation of the Urganian carbonate host rocks led to flows inducing  
521 dissolution of MF3 grains in the host rock. This phase produced the moldic porosity and  
522 increased the porosity/permeability (Step 8 on Fig. 9B and C). These fluids, however, did not  
523 affect fault zones.

## 524 2. EVOLUTION OF FAULT ZONES RESERVOIR PROPERTIES

525 The host rock presents a monophasic evolution and switch from a type IV reservoir where  
526 matrix provided storage and flow, to a type III reservoir where fractures behave as pathways  
527 towards fluid flow but the production comes mainly from the matrix (Nelson 2001, Fig. 10A).  
528 The fault zones present a more complex polyphasic evolution than the host rock. Indeed, their  
529 reservoir properties evolved from a type IV reservoir corresponding to the host rock to a type I  
530 reservoir where fractures provide both storage and flow pathways (Nelson 2001, Fig. 10A).  
531 Both fault zones present slight differences. The Castellás fault zone was completely tight soon  
532 after C3 cementation. Consequently, it did not fit to the Nelson reservoir type classification.  
533 However, after fault core formation, the fault zone presents a high fault core permeability. In  
534 this study we propose a new approach with a triangle diagram taking into account fault core  
535 permeability to remove the flaws of this method (Fig. 10B). The percentage assigned to the  
536 fault core or to the matrix are qualitatively estimated. Further quantification could be evaluated,  
537 for instance, with the width of the fault core and damage zone domains, or by estimating the  
538 fracture network volume. However, no recent study have provided such quantification. Thus,  
539 for Castellás fault zone, permeability evolves from a stage with exclusive contribution from the  
540 host rock permeability (100% matrix; step 0 on Fig. 10B) to a permeability due to 50% to the



541 matrix and 50% to the fault core during dilation band development (step 2 on Fig. 10B).  
 542 Thereafter, during the two



543  
 544 **Figure 10** : Castellias and D19 fault zone reservoir properties evolution. A: evolution of permeability and porosity taking into  
 545 account fault zone fractures and matrix after Nelson (2001) and B: Triangle diagram of permeability evolution with 3  
 546 components: matrix, fractures and fault core. Numbers 1 to 8 correspond to the steps 1 to 8(see text for description). K:  
 547 Permeability,  $\Phi$ : porosity, FZ: Fault Zone, DZ: Damage zone, MF1 and MF3: Micrite micro-fabric.

548 fracture events permeability is mainly linked to fracturing (C2: 30% fault core, 70% fractures;  
 549 C3: 15% fault core, 15% matrix, 70% fractures; step 3, 4 on Fig. 10B). Then, after fault core  
 550 formation and during dolomitization event, permeability is solely provided by the fault core  
 551 (step 6, 7 on Fig. 10B). Lastly, after fault zone reactivation, the permeability is due to 20% to  
 552 the fault core and 80% to fractures (step 7c on Fig. 10B). The D19 fault zone permeability  
 553 during its development was related for 20% to the matrix, 20% to the fractures and 60% to the  
 554 fault core (step 7a and 7b on Fig. 10B).

## 555 8. CONCLUSION

556 This study deciphered the diagenetic evolution of two fault zones and the impact on reservoir  
 557 properties of both faults and host rock in the frame of the overall geodynamic context of the SE  
 558 Basin. The main outcomes are:

- 559 • Fault zones may have a complex diagenetic history, but most diagenetic phases occur  
 560 during the nucleation of the fault. In the case of Castellias fault zone, the diagenetic  
 561 imprint is mainly influenced by early diagenesis occurring along fractures and diffuse  
 562 dilation zones prior to the proper fault plane nucleation. Regarding D19 fault zone, most  
 563 of diagenetic alterations occurred just after fault onset in the first stage of its activity. In  
 564 both cases, the cementation altered initial reservoir properties in the fault zone vicinity,  
 565 switching from type III to type I during the first stages of fault development. Later fault  
 566 reactivation slightly impacts matrix porosity/permeability.
- 567 • Fault zones act as drains canalizing fluid flows in the beginning of their development.  
 568 This induces fault zone cementation but preservation of host rock microporosity. This  
 569 important fluid drainage is visible on D19 outcrop where the flowing fluids led to  
 570 dissolution/cementation of fault rock matrix and formed karsts.

571 • All diagenetic stages, including cementation and dolomitization, result from low-  
572 temperature fluids with important meteoric water input. These low-temperature fluid  
573 flows associated with the deformation and cementation types and, the lack of  
574 mineralisation specific to high-temperature fluids disprove any significant hydrothermal  
575 influence.

576 This regional study allows to draw broader rules for complex faults with polyphasic activity  
577 affecting granular carbonates at shallow burial conditions (Fig. 9).

- 578 • Under extensional context, fault nucleation can lead to the development of dilation  
579 bands acting as conduits for fluid flow. Carbonates are very sensitive to rock-fluids  
580 interactions. Thus, the onset of dilation bands triggers important diagenetic reactions  
581 that strongly alter local reservoir properties. During later fault zone development, the  
582 diagenesis depends on faults zones internal architecture.
- 583 • Fracture networks related to fault nucleation in granular carbonates form good fluid  
584 pathways before proper fault plane formation. However, in the case of pre-fractured  
585 carbonates, like D19 fault zone, fault rocks early appear in fault cores. In these cases,  
586 fluids flowed preferentially within the permeable breccia rather than the damage zone.

587

## 588 **Acknowledgement**

589 We would like to thank Suzan Verdegaal, Lionel Marié and Alain Tonetto for support they  
590 provide during this study. We grateful to Editor Kei Ogata, and Fabrizio Agosta, Mattia Pizzati  
591 and Eric Salomon who made critical suggestions to improve this paper.  
592

- 594 Agosta, F., Prasad, M. and Aydin, A.: Physical properties of carbonate fault rocks, Fucino Basin (Central Italy):  
 595 implications for fault seal in platform carbonates, *Geofluids*, 7, 19–32, doi:10.1111/j.1468-8123.2006.00158.x,  
 596 2007.
- 597 Agosta, F., Mulch, A., Chamberlain, P. and Aydin, A.: Geochemical traces of CO<sub>2</sub>-rich fluid flow along normal  
 598 faults in central Italy, *Geophys. J. Int.*, 174(2), 1074–1096, doi:10.1111/j.1365-246X.2008.03792.x, 2008.
- 599 Agosta, F., Alessandrini, M., Antonellini, M., Tondi, E. and Giorgioni, M.: From fractures to flow: A field-based  
 600 quantitative analysis of an outcropping carbonate reservoir, *Tectonophysics*, 490(3–4), 197–213,  
 601 doi:10.1016/j.tecto.2010.05.005, 2010.
- 602 Agosta, F., Ruano, P., Rustichelli, A., Tondi, E., Galindo-Zaldívar, J. and Sanz de Galdeano, C.: Inner structure  
 603 and deformation mechanisms of normal faults in conglomerates and carbonate grainstones (Granada Basin, Betic  
 604 Cordillera, Spain): Inferences on fault permeability, *J. Struct. Geol.*, 45, 4–20, doi:10.1016/j.jsg.2012.04.003,  
 605 2012.
- 606 Alikarami, R. and Torabi, A.: Geomechanics for Energy and the Environment Micro-texture and petrophysical  
 607 properties of dilation and compaction shear bands in sand, *Geomech. Energy Environ.*, 3, 1–10,  
 608 doi:10.1016/j.gete.2015.06.001, 2015.
- 609 Allan, J. R. and Matthews, R. K.: Isotope signatures associated with early meteoric diagenesis, *Sedimentology*,  
 610 29(6), 797–817, doi:10.1111/j.1365-3091.1982.tb00085.x, 1982.
- 611 Allmendinger, R. W., Cardozo, N. and Fisher, D. M.: Structural geology algorithms: Vectors and tensors,  
 612 Cambridge Univ. Press, 9781107012, 1–289, doi:10.1017/CBO9780511920202, 2013.
- 613 Anglada, R., Arlhac, P., Catzigras, F., Colomb, E., Damiani, L., Durand, J. P., Durozoy, G., Guieu, G., Masse, J.  
 614 P., Nury, D., Philip, J., Rouire, J., Rousset, C., Roux, R. M. and Blanc, J. J.: Notice explicative. Carte géologique  
 615 de la France a 1/50 000. Martigues - Marseille., 1977.
- 616 Aubert, I., Lamarche, J. and Léonide, P.: Deciphering background fractures from damage fractures in fault zones  
 617 and their effect on reservoir properties in microporous carbonates (Urgonian limestones, SE France), *Pet. Geosci.*,  
 618 doi:DOI10.1144/petgeo2019-010, 2019a.
- 619 Aubert, I., Lamarche, J., Richard, P. and Leonide, P.: Imbricated Structure and Hydraulic Path Induced by Strike  
 620 Slip Reactivation of a Normal Fault in Carbonates, in Fifth International Conference on Fault and Top Seals, p. 4.,  
 621 2019b.
- 622 Bense, V. F., Gleeson, T., Loveless, S. E., Bour, O. and Scibek, J.: Fault zone hydrogeology, *Earth-Science Rev.*,  
 623 127, 171–192, doi:10.1016/j.earscirev.2013.09.008, 2013.
- 624 Bernard, X. Du, Eichhubl, P. and Aydin, A.: Dilation bands : A new form of localized failure in granular media,  
 625 29(24), 1–4, doi:10.1029/2002GL015966, 2002.
- 626 Besson, D.: Architecture du bassin rhodano-provençal miocène (Alpes , SE France) : relations entre déformation,  
 627 physiographie et sédimentation dans un bassin molassique d'avant-pays, Ecole des Mines, Paris., 2005.
- 628 Bestani, L.: Géométrie et cinématique de l'avant-pays provençal : Modélisation par coupes équilibrées dans une  
 629 zone à tectonique polyphasée, Aix-Marseille University, 2015.
- 630 Bestani, L., Espurt, N., Lamarche, J., Bellier, O. and Hollender, F.: Reconstruction of the Provence Chain  
 631 evolution, Southeastern France, *Tectonics*, 35, 1506–1525, doi:10.1002/2016TC004115, 2016.
- 632 Billi, A., Salvini, F. and Storti, F.: The damage zone-fault core transition in carbonate rocks: Implications for fault  
 633 growth, structure and permeability, *J. Struct. Geol.*, 25(11), 1779–1794, doi:10.1016/S0191-8141(03)00037-3,  
 634 2003.
- 635 Billi, A., Primavera, P., Soligo, M. and Tuccimei, P.: Minimal mass transfer across dolomitic granular fault cores,  
 636 *Geochemistry, Geophys. Geosystems*, 9(1), doi:10.1029/2007GC001752, 2008.
- 637 Borgomano, J., Masse, J., Maskiry, S. Al, Borgomano, J. and International, S.: The lower Aptian Shuaiba carbonate  
 638 outcrops in Jebel Akhdar, northern Oman: Impact on static modeling for Shuaiba petroleum reservoirs, *Bull. Am.*  
 639 *Assoc. Pet. Geol.*, 9(9), 1513–1529, doi:10.1306/61EEDCE2-173E-11D7-8645000102C1865D, 2002.
- 640 Borgomano, J., Masse, J. P., Fenerci-Masse, M. and Fournier, F.: Petrophysics of lower cretaceous platform  
 641 carbonate outcrops in provence (SE France): Implications for carbonate reservoir characterisation, *J. Pet. Geol.*,  
 642 36(1), 5–41, doi:10.1111/jpg.12540, 2013.
- 643 Bruna, P., Guglielmi, Y., Viseur, S., Lamarche, J. and Bildstein, O.: Coupling fracture facies with in-situ  
 644 permeability measurements to generate stochastic simulations of tight carbonate aquifer properties: Example from  
 645 the Lower Cretaceous aquifer , Northern Provence , SE France, *J. Hydrol.*, 529, 737–753,  
 646 doi:10.1016/j.jhydrol.2015.08.054, 2015.
- 647 Buschkuehle, B. E. and Machel, H. G.: Diagenesis and paleo fluid flow in the Devonian Southesk-Cairn carbonate  
 648 complex in Alberta, Canada, *Mar. Pet. Geol.*, 19, 219–227, doi:10.1016/S0264-8172(02)00014-4, 2002.
- 649 Caine, J. S., Evans, J. P. and Forster, C. B.: Fault zone architecture and permeability structure, *Geology*, 24(11),  
 650 1025–1028, doi:10.1130/0091-7613(1996)024<1025, 1996.
- 651 Cardozo, N. and Allmendinger, N. W.: Spherical projections with OSX Stereonets, *Comput. Geosci.*, 51, 193–205,

652 doi:10.1016/j.cageo.2012.07.021, 2013.

653 Celico, F., Petrella, E. and Celico, P.: Hydrogeological behaviour of some fault zones in a carbonate aquifer of  
654 Southern Italy: An experimentally based model, *Terra Nov.*, 18(5), 308–313, doi:10.1111/j.1365-  
655 3121.2006.00694.x, 2006.

656 Champion, C., Choukroune, P. and Clauzon, G.: La déformation post-miocène en provence occidentale, *Geodin.*  
657 *Acta*, 13(2–3), 67–85, doi:10.1080/09853111.2000.11105365, 2000.

658 Chester, F. M. and Logan, J. M.: Implications for Mechanical Properties of Brittle Faults from Observations of the  
659 Punchbowl Fault Zone, California, *PAGEOPH*, 124(1/2), 79, doi:10.1007/BF00875720, 1986.

660 Chester, F. M. and Logan, J. M.: Composite planar fabric of gouge from the Punchbowl Fault, California, *J. Struct.*  
661 *Geol.*, 9(5–6), doi:10.1016/0191-8141(87)90147-7, 1987.

662 Delle Piane, C., Giwelli, A., Clennell, M. Ben, Esteban, L., Nogueira Kiewiet, M. C. D., Kiewiet, L., Kager, S.  
663 and Raimon, J.: Frictional and hydraulic behaviour of carbonate fault gouge during fault reactivation — An  
664 experimental study, *Tectonophysics*, 690(PartA), 21–34, doi:10.1016/j.tecto.2016.07.011, 2016.

665 Deming, D., Nunn, A. and Evans, D. G.: Thermal Effects of Compaction-Driven Groundwater Flow, 95(89), 6669–  
666 6683, doi:10.1029/JB095iB05p06669, 1990.

667 Demory, F. R., Conesa, G. I., Oudet, J. U., Mansouri, H. A. and Münch, P. H.: Magnetostratigraphy and  
668 paleoenvironments in shallow-water carbonates : The Oligocene- Miocene sediments of the northern margin of the  
669 Liguro- Provençal basin ( West Marseille , southeastern France), *Bull. Soc. géol. Fr.*, 1, 37–55,  
670 doi:10.2113/gssgfbull.182.1.37, 2011.

671 Deville de Periere, M., Durllet, C., Vennin, E., Lambert, L., Bourillot, R., Caline, B. and Poli, E.: Morphometry of  
672 micrite particles in cretaceous microporous limestones of the middle east: Influence on reservoir properties, *Mar.*  
673 *Pet. Geol.*, 28(9), 1727–1750, doi:10.1016/j.marpetgeo.2011.05.002, 2011.

674 Deville de Periere, M., Durllet, C., Vennin, E., Caline, B., Boichard, R. and Meyer, A.: Influence of a major  
675 exposure surface on the development of microporous micritic limestones - Example of the Upper Mishrif  
676 Formation (Cenomanian) of the Middle East, *Sediment. Geol.*, 353, 96–113, doi:10.1016/j.sedgeo.2017.03.005,  
677 2017.

678 Dorobek, S.: migration of orogenic fluids through the Siluro-Devonian Helderberg Group during late Paleozoic  
679 deformation: constraints on fluid sources and implications for thermal histories of sedimentary basins presence, ,  
680 159, 25–45, doi:10.1016/0040-1951(89)90168-6, 1989.

681 Eltom, H. A., Gonzalez, L. A., Hasiotis, S. T., Rankey, E. C. and Cantrell, D. L.: Paleogeographic and paleo-  
682 oceanographic influences on carbon isotope signatures: Implications for global and regional correlation, Middle-  
683 Upper Jurassic of Saudi Arabia, *Sediment. Geol.*, 364, 89–102, doi:10.1016/j.sedgeo.2017.12.011, 2018.

684 Espurt, N., Hippolyte, J. C., Saillard, M. and Bellier, O.: Geometry and kinematic evolution of a long-living  
685 foreland structure inferred from field data and cross section balancing, the Sainte-Victoire System, Provence,  
686 France, *Tectonics*, 31(4), doi:10.1029/2011TC002988, 2012.

687 Evans, J. P., Forster, C. B. and Goddard, J. V.: Permeability of fault-related rocks, and implications for hydraulic  
688 structure of fault zones, *J. Struct. Geol.*, 19(11), 1393–1404, doi:10.1016/S0191-8141(97)00057-6, 1997.

689 Ferraro, F., Agosta, F., Ukar, E., Grieco, D. S., Cavalcante, F., Belviso, C. and Prosser, G.: Structural diagenesis  
690 of carbonate fault rocks exhumed from shallow crustal depths: An example from the central-southern Apennines,  
691 Italy, *J. Struct. Geol.*, 122(February), 58–80, doi:10.1016/j.jsg.2019.02.008, 2019.

692 Florida, S., Maliva, R. G., Missimer, T. M., Clayton, E. A. and Dickson, J. A. D.: Diagenesis and porosity  
693 preservation in Eocene microporous limestones , *Sediment. Geol.*, 217(1–4), 85–94,  
694 doi:10.1016/j.sedgeo.2009.03.011, 2009.

695 Ford, M., Duchene, S., Gasquet, D. and Vanderhaeghe, O.: Two-phase orogenic convergence in the external and  
696 internal SW Alps, *J. Geol. Soc. London.*, 163(5), 815–826, doi:10.1144/0016-76492005-034, 2006.

697 Fossen, H. and Bale, A.: Deformation bands and their influence on fluid flow, 12(12), 1685–1700,  
698 doi:10.1306/07300706146, 2007.

699 Fossen, H. and Rotevatn, A. Fault linkage and relay structures in extensional settings — A review, *Earth Sci. Rev.*,  
700 154, 14–28, doi:10.1016/j.earscirev.2015.11.014, 2016.

701 Fouke, B. W., Everts, A. W., Zwart, E. W. and Schlager, W.: Subaerial exposure unconformities on the Vercors  
702 carbonate platform (SE France) and their sequence stratigraphic significance, *Geol. Soc. London, Spec. Publ.*, 104,  
703 295–319, 1996.

704 Fournier, F. and Borgomano, J.: Critical porosity and elastic properties of microporous mixed carbonate-  
705 siliciclastic rocks, *Geophysics*, 74(2), E93–E109, doi:10.1190/1.3043727, 2009.

706 Fournier, F., Leonide, P., Biscarrat, K., Gallois, A., Borgomano, J. and Foubert, A.: Elastic properties of  
707 microporous cemented grainstones, *Geophysics*, 76(6), E211–E226, doi:10.1190/geo2011-0047.1, 2011.

708 Gattacceca, J., Deino, A., Rizzo, R., Jones, D. S., Henry, B., Beaudoin, B. and Vadeboin, F.: Miocene rotation of  
709 Sardinia: New paleomagnetic and geochronological constraints and geodynamic implications, *Earth Planet. Sci.*  
710 *Lett.*, 258(3–4), 359–377, doi:10.1016/j.epsl.2007.02.003, 2007.

711 Gaviglio, P., Bekri, S., Vanduycke, S., Adler, P. M., Schroeder, C., Bergerat, F., Darquennes, A. and Coulon, M.:

712 Faulting and deformation in chalk, *J. Struct. Geol.*, 31(2), 194–207, doi:10.1016/j.jsg.2008.11.011, 2009.

713 Gisquet, F., Lamarche, J., Floquet, M., Borgomano, J., Masse, J. P. and Caline, B.: Three-dimensional structural  
714 model of composite dolomite bodies in folded area (upper Jurassic of the Etoile massif, southeastern France), *Am.*  
715 *Assoc. Pet. Geol. Bull.*, 97(9), 1477–1501, doi:10.1306/04021312016, 2013.

716 Godet, A., Bodin, S., Föllmi, K. B., Vermeulen, J., Gardin, S., Fiet, N., Adatte, T., Berner, Z., Stüben, D. and van  
717 de Schootbrugge, B.: Evolution of the marine stable carbon-isotope record during the early Cretaceous: A focus  
718 on the late Hauterivian and Barremian in the Tethyan realm, *Earth Planet. Sci. Lett.*, 242(3–4), 254–271,  
719 doi:10.1016/j.epsl.2005.12.011, 2006.

720 Guendon, J.-L. and Parron, C.: Les phenomenes karstiques dans les processus de la bauxitisation sur substrat  
721 carbonate. Exemple de gisement du sud est de la France, *Ann. la Société Géologique Belgique*, 108, 85–92, 1985.

722 Guieu, G.: Un exemple de tectonique tangentielle: l'évolution du cadre montagneux de Marseille, *Bull. la Société*  
723 *Géologique Fr.*, 7 (T.IX N°), 610–630, 1967.

724 Guyonnet-Benaize, C., Lamarche, J., Masse, J. P., Villeneuve, M. and Viseur, S.: 3D structural modelling of small-  
725 deformations in poly-phase faults pattern. Application to the Mid-Cretaceous Durance uplift, Provence (SE  
726 France), *J. Geodyn.*, 50(2), 81–93, doi:10.1016/j.jog.2010.03.003, 2010.

727 Hammond, K. J. and Evans, J. P.: Geochemistry, mineralization, structure, and permeability of a normal- fault  
728 zone, Casino mine, Alligator Ridge district, north central Nevada, 25, 717–736, doi:10.1016/S0191-  
729 8141(02)00060-3, 2003.

730 Heiland, J., Raab, S. and Potsdam, G.: Experimental Investigation of the Influence of Differential Stress on  
731 Permeability of a Lower Permian ( Rotliegend ) Sandstone Deformed in the Brittle Deformation, *Phys. Chem.*  
732 *earth*, 26(1), 33–38, doi:10.1016/S1464-1895(01)00019-9, 2001.

733 Hodson, K. R., Crider, J. G. and Huntington, K. W.: Temperature and composition of carbonate cements record  
734 early structural control on cementation in a nascent deformation band fault zone: Moab Fault, Utah, USA,  
735 *Tectonophysics*, 690, 240–252, doi:10.1016/j.tecto.2016.04.032, 2016.

736 Hollis, C., Vahrenkamp, V., Tull, S., Mookerjee, A. and Taberner, C.: Pore system characterisation in  
737 heterogeneous carbonates: An alternative approach to widely-used rock-typing methodologies, *Mar. Pet. Geol.*,  
738 27(4), 772–793, doi:10.1016/j.marpetgeo.2009.12.002, 2010.

739 Kaminskaite, I., Fisher, Q. J. and Michie, E. A. H.: Microstructure and petrophysical properties of deformation  
740 bands in high porosity carbonates, *J. Struct. Geol.*, 119(November 2018), 61–80, doi:10.1016/j.jsg.2018.12.001,  
741 2019.

742 Kim, Y. S., Peacock, D. C. P. and Sanderson, D. J.: Fault damage zones, *J. Struct. Geol.*, 26(3), 503–517,  
743 doi:10.1016/j.jsg.2003.08.002, 2004.

744 Knipe, R. J.: The influence of fault zone processes and diagenesis on fluid flow, *Diagenes. basin Dev. AAPG Stud.*  
745 *Geol.*, 36, 135–154 [online] Available from:  
746 <http://archives.datapubs.com/data/specpubs/resmi1/data/a067/a067/0001/0100/0135.htm>, 1993.

747 Knipe, R. J., Jones, G. and Fisher, Q. J.: Faulting, fault sealing and fluid flow in hydrocarbon reservoirs: an  
748 introduction, *Geol. Soc. London, Spec. Publ.*, 147(1), NP LP-NP, doi:10.1144/GSL.SP.1998.147.01.21, 1998.

749 Lamarche, J., Lavenue, A. P. C., Gauthier, B. D. M., Guglielmi, Y. and Jayet, O.: Relationships between fracture  
750 patterns, geodynamics and mechanical stratigraphy in Carbonates (South-East Basin, France), *Tectonophysics*,  
751 581, 231–245, doi:10.1016/j.tecto.2012.06.042, 2012.

752 Lambert, L., Durllet, C., Loreau, J. P. and Marnier, G.: Burial dissolution of micrite in Middle East carbonate  
753 reservoirs (Jurassic-Cretaceous): Keys for recognition and timing, *Mar. Pet. Geol.*, 23(1), 79–92,  
754 doi:10.1016/j.marpetgeo.2005.04.003, 2006.

755 Laubach, S. E., Eichhubl, P., Hilgers, C. and Lander, R. H.: Structural diagenesis, *J. Struct. Geol.*, 32(12), 1866–  
756 1872, doi:10.1016/j.jsg.2010.10.001, 2010.

757 Lavenue, A. P. C., Lamarche, J., Gallois, A. and Gauthier, B. D. M.: Tectonic versus diagenetic origin of fractures  
758 in a naturally fractured carbonate reservoir analog [Nerthe anticline, Southeastern France, *Am. Assoc. Pet. Geol.*  
759 *Bull.*, 97(12), 2207–2232, doi:10.1306/04041312225, 2013.

760 Leonide, P., Borgomano, J., Masse, J. and Doublet, S.: Relation between stratigraphic architecture and multi-scale  
761 heterogeneities in carbonate platforms: The Barremian – lower Aptian of the Monts de Vaucluse, SE France,  
762 *Sediment. Geol.*, 265–266, 87–109, doi:10.1016/j.sedgeo.2012.03.019, 2012.

763 Léonide, P., Fournier, F., Reijmer, J. J. G., Vonhof, H., Borgomano, J., Dijk, J., Rosenthal, M., Van Goethem, M.,  
764 Cochard, J. and Meulenaars, K.: Diagenetic patterns and pore space distribution along a platform to outer-shelf  
765 transect (Urgonian limestone, Barremian-Aptian, SE France), *Sediment. Geol.*, 306, 1–23,  
766 doi:10.1016/j.sedgeo.2014.03.001, 2014.

767 Long, J. J. and Imber, J.: Geological controls on fault relay zone scaling, *J. Struct. Geol.*, 33(12), 1790–1800,  
768 doi:10.1016/j.jsg.2011.09.011, 2011.

769 Lothe, A. E., Gabrielsen, R. H., Hagen, N. B. and Larsen, B. T.: An experimental study of the texture of  
770 deformation bands: effects on the porosity and permeability of sandstones, (1990), doi:10.1144/petgeo.8.3.195,  
771 2002.

772 Lucia, F. J.: Origin and petrophysics of dolostone pore space, *Geom. Petrog. Dolomite Hydrocarb. Reserv. Geol.*  
773 *Soc. London, Spec. Publ.*, 235, 141–155, doi:10.1144/GSL.SP.2004.235.01.06, 2004.

774 Machel, H. G.: Concepts and models of dolomitization: a critical reappraisal, *Geol. Soc. London, Spec. Publ.*,  
775 235(1), 7–63, doi:10.1144/GSL.SP.2004.235.01.02, 2004.

776 Machel, H. G., Cavell, P. A., Buschkuehle, B. E. and Michael, K.: Tectonically induced fluid flow in Devonian  
777 carbonate aquifers of the Western Canada Sedimentary Basin, *Journal geochemical Explor.*, 70, 213–217,  
778 doi:10.1016/S0375-6742(00)00093-5, 2000.

779 Main, I. G., Kwon, O., Ngwenya, B. T. and Elphick, S. G.: Fault sealing during deformation-band growth in porous  
780 sandstone, *Geology*, 28(12), 1131–1134, doi:10.1130/0091-7613(2000)28<1131:FSDDGI>2.0.CO;2, 2000.

781 Masse, J.-P. and Philip, J.: Paléogéographie et tectonique du Crétacé moyen en Provence: révision du concept  
782 d'isthme durancien., *Rev. Géographie Phys. Géologie Dyn.*, 18(1), 49–46, 1976.

783 Masse, J. P.: Les calcaires urgoniens de Provence (Valanginien-Aptien Inférieur) - Stratigraphie, paléontologie,  
784 paléoenvironnements et leur évolution, Marseille, Thèse de la Faculté des Sciences de Luminy (U2), 1976.

785 Masse, J. P. and Fenerci-Masse, M.: Carbonate production by rudist bivalves. The record of Late Barremian  
786 requieniid communities from Provence (SE France), *Palaeogeogr. Palaeoclimatol. Palaeoecol.*, 234(2–4), 239–  
787 257, doi:10.1016/j.palaeo.2005.10.010, 2006.

788 Masse, J. P. and Fenerci Masse, M.: Drowning discontinuities and stratigraphic correlation in platform carbonates.  
789 The late Barremian-early Aptian record of southeast France, *Cretac. Res.*, 32(6), 659–684,  
790 doi:10.1016/j.cretres.2011.04.003, 2011.

791 Matonti, C., Lamarche, J., Guglielmi, Y. and Marié, L.: Structural and petrophysical characterization of mixed  
792 conduit/seal fault zones in carbonates: Example from the Castellans fault (SE France), *J. Struct. Geol.*, 39, 103–  
793 121, doi:10.1016/j.jsg.2012.03.003, 2012.

794 Micarelli, L., Benedicto, A. and Wibberley, C. A. J.: Structural evolution and permeability of normal fault zones  
795 in highly porous carbonate rocks, *J. Struct. Geol.*, 28(7), 1214–1227, doi:10.1016/j.jsg.2006.03.036, 2006.

796 Molli, G., Cortecchi, G., Vaselli, L., Ottria, G., Cortopassi, A., Dinelli, E., Mussi, M. and Barbieri, M.: Fault zone  
797 structure and fluid–rock interaction of a high angle normal fault in Carrara marble (NW Tuscany, Italy), *J. Struct.*  
798 *Geol.*, 32(9), 1334–1348, doi:10.1016/j.jsg.2009.04.021, 2010.

799 Molliex, S., Bellier, O., Terrier, M., Lamarche, J., Martelet, G. and Espurt, N.: Tectonic and sedimentary  
800 inheritance on the structural framework of Provence (SE France): Importance of the Salon-Cavaillon fault,  
801 *Tectonophysics*, 501(1–4), 1–16, doi:10.1016/j.tecto.2010.09.008, 2011.

802 Moss, S. and Tucker, M. E.: Diagenesis of Barremian-Aptian platform carbonates (the Urganian Limestone  
803 Formation of SE France): near-surface and shallow-burial diagenesis, *Sedimentology*, 42(6), 853–874,  
804 doi:10.1111/j.1365-3091.1995.tb00414.x, 1995.

805 Mozley, P. S. and Goodwin, L. B.: Patterns of cementation along a Cenozoic normal fault: a record of paleoflow  
806 orientations, *Geology*, 23(6), 539–542, doi:10.1130/0091-7613(1995)023<0539:POCAAC>2.3.CO;2, 1995.

807 Nelson, R.: *Geologic Analysis of Naturally Fractured Reservoirs*, second ed., 2001.

808 Ostwald, W.: *Lehrbuch der allgemeinen Chemie*, Verlag von Wilhelm Engelmann, Leipzig, 2, 909, 1886.

809 Philip, J.: Les formations calcaires à rudistes du Crétacé supérieur provençal et rhodanien, Thèse de Doctorat,  
810 Université de Provence (Marseille), 1970.

811 Le Pichon, X., Bergerat, F. and Roulet, M.-J.: Plate kinematics and tectonics leading to the Alpine belt formation;  
812 A new analysis, *Geol. Soc. Am.*, 218(March 1986), 111–131, doi:10.1130/SPE218-p111, 1988.

813 Pichon, X. Le, Rangin, C., Hamon, Y., Loget, N., Lin, J. Y., Andreani, L. and Flotte, N.: Geodynamics of the  
814 France southeast basin, *Bull. la Soc. Geol. Fr.*, 181(6), 477–501, doi:10.2113/gssgfbull.181.6.477, 2010.

815 Purser, B. H.: Sédimentation et diagenèse des carbonates néritiques récents, *Les éléments de la sédimentation et*  
816 *de la diagenèse*, Ed. Tech., 1, 366, 1980.

817 Reches, Z. and Dewers, T. A.: Gouge formation by dynamic pulverization during earthquake rupture, *Earth Planet.*  
818 *Sci. Lett.*, 235(1–2), 361–374, doi:10.1016/j.epsl.2005.04.009, 2005.

819 Reid, R. P. and Macintyre, I. G.: Microboring Versus Recrystallization: Further Insight into the Micritization  
820 Process, *J. Sediment. Res.*, 70(May), 24–28, doi:10.1306/2DC408FA-0E47-11D7-8643000102C1865D, 2000.

821 Roche, V.: Analyse structurale et géo-mécanique de réseau de failles du chaînon de La Fare les Oliviers (Provence),  
822 *Univ. Montpellier 2*, 45, 2008.

823 Rossetti, F., Aldega, L., Tecce, F., Balsamo, F., Billi, A. and Brilli, M.: Fluid flow within the damage zone of the  
824 Boccheggiano extensional fault (Larderello-Travale geothermal field, central Italy): Structures, alteration and  
825 implications for hydrothermal mineralization in extensional settings, *Geol. Mag.*, 148(4), 558–579,  
826 doi:10.1017/S001675681000097X, 2011.

827 Saller, A. H. and Henderson, N.: Distribution of Porosity and Permeability in Platform Dolomites: Insight from  
828 the Permian of West Texas: reply, *Am. Assoc. Pet. Geol. Bull.*, 85, 530–532, doi:10.1306/090800850530, 2001.

829 Sallier, B.: Carbonates microporeux: influence de l'architecture du milieu poreux et de la mouillabilité sur les  
830 écoulements diphasiques dans les réservoirs pétroliers, *Univ. Genève.*, 2005.

831 Samankassou, E., Tresch, J. and Strasser, A.: Origin of peloids in Early Cretaceous deposits, Dorset, South

832 England, Facies, 51(1–4), 264–273, doi:10.1007/s10347-005-0002-8, 2005.

833 Séranne, M.: The Gulf of Lion continental margin (NW Mediterranean) revisited by IBS: an overview, *Geol. Soc.*  
834 *London, Spec. Publ.*, 156(1), 15–36, doi:10.1144/GSL.SP.1999.156.01.03, 1999.

835 Sibley, D. F. and Gregg, J. A. Y. M.: Classification of Dolomite Rock Texture, *J. Sediment. Petrol.*, 57(6), 967–  
836 975, doi:10.1306/212F8CBA-2B24-11D7-8648000102C1865D, 1987.

837 Sibson, R. H.: Crustal stress, faulting and fluid flow, *Geol. Soc. London, Spec. Publ.*, 78(1), 69–84,  
838 doi:10.1144/GSL.SP.1994.078.01.07, 1994.

839 Sibson, R. H.: Structural permeability of fluid-driven fault-fracture meshes, *J. Struct. Geol.*, 18(8), 1031–1042,  
840 doi:10.1016/0191-8141(96)00032-6, 1996.

841 Sinisi, R., Petrullo, A. V., Agosta, F., Paternoster, M., Belviso, C. and Grassa, F.: Contrasting fault fluids along  
842 high-angle faults: a case study from Southern Apennines (Italy), *Tectonophysics*, 690(PartA), 206–218,  
843 doi:10.1016/j.tecto.2016.07.023, 2016.

844 Solum, J. G. and Huisman, B. A. H.: Toward the creation of models to predict static and dynamic fault-seal  
845 potential in carbonates, *Pet. Geosci.*, 23(1), 70–91, doi:10.1144/petgeo2016-044, 2016.

846 Solum, J. G., Davatzes, N. C. and Lockner, D. A.: Fault-related clay authigenesis along the Moab Fault:  
847 Implications for calculations of fault rock composition and mechanical and hydrologic fault zone properties, *J.*  
848 *Struct. Geol.*, 32(12), 1899–1911, doi:10.1016/j.jsg.2010.07.009, 2010.

849 Storti, F., Billi, A. and Salvini, F.: Particle size distributions in natural carbonate fault rocks: Insights for non-self-  
850 similar cataclasis, *Earth Planet. Sci. Lett.*, 206(1–2), 173–186, doi:10.1016/S0012-821X(02)01077-4, 2003.

851 Swart, P. K.: The geochemistry of carbonate diagenesis: The past, present and future, *Sedimentology*, 62(5), 1233–  
852 1304, doi:10.1111/sed.12205, 2015.

853 Tempier, C.: Modèle nouveau de mise en place des structures provençales, *Bull. la Soc. Geol. Fr.*, 3, 533–540,  
854 doi:10.2113/gssgfbull.III.3.533, 1987.

855 Tondi, E.: Nucleation, development and petrophysical properties of faults in carbonate grainstones: Evidence from  
856 the San Vito Lo Capo peninsula (Sicily, Italy), *J. Struct. Geol.*, 29(4), 614–628, doi:10.1016/j.jsg.2006.11.006,  
857 2007.

858 Triat, J.: Paléoaaltérations dans le crétacé supérieur de Provence rhodanienne, *Strasbourg: Institut de Géologie –*  
859 *Université Louis-Pasteur.*, 1982.

860 Vincent, B., Emmanuel, L., Houel, P. and Loreau, J. P.: Geodynamic control on carbonate diagenesis: Petrographic  
861 and isotopic investigation of the Upper Jurassic formations of the Paris Basin (France), *Sediment. Geol.*, 197(3–  
862 4), 267–289, doi:10.1016/j.sedgeo.2006.10.008, 2007.

863 Volery, C., Davaud, E., Foubert, A. and Caline, B.: Shallow-marine microporous carbonatereservoir rocks in the  
864 Middle East: relationship with seawater Mg/Ca ration and eustatic sea level, *J. Pet. Geol.*, 32(October), 313–325,  
865 doi:10.1111/j.1747-5457.2009.00452.x, 2009.

866 Volery, C., Davaud, E., Foubert, A. and Caline, B.: Lacustrine microporous micrites of the Madrid Basin (Late  
867 Miocene, Spain) as analogues for shallow-marine carbonates of the Mishrif reservoir formation (Cenomanian to  
868 Early Turonian, Middle East), *Facies*, 56(3), 385–397, doi:10.1007/s10347-009-0210-8, 2010.

869 Walsh, J. J., Watterson, J., Bailey, W. R. and Childs, C.: Fault relays, bends and branch-lines, 21(8–9), 1019–  
870 1026, doi:10.1016/S0191-8141(99)00026-7, 1999.

871 Walsh, J. J., Bailey, W. R., Childs, C., Nicol, A. and Bonson, C. G.: Formation of segmented normal faults: a 3-D  
872 perspective, 25, 1251–1262, doi:10.1016/S0191-8141(02)00161-X, 2003.

873 Wilkins, S. J., Naruk, S. J., Wilkins, S. J., International, S., Naruk, S. J. and International, S.: Quantitative analysis  
874 of slip-induced dilation with application to fault seal, 1(1), 97–113, doi:10.1306/08010605177, 2007.

875 Woodcock, N. H., Dickson, J. A. D. and Tarasewicz, J. P. T.: Transient permeability and reseal hardening in fault  
876 zones: evidence from dilation breccia textures, *Geol. Soc. London, Spec. Publ.*, 270, 43–53, 2007.

877 Wu, G., Gao, L., Zhang, Y., Ning, C. and Xie, E.: Fracture attributes in reservoir-scale carbonate fault damage  
878 zones and implications for damage zone width and growth in the deep subsurface, *J. Struct. Geol.*, 118(February  
879 2017), 181–193, doi:10.1016/j.jsg.2018.10.008, 2019.

880 Zhang, Y., Schaub, P. M., Zhao, C., Ord, A., Hobbs, B. E. and Barnicoat, A. C.: Fault-related dilation,  
881 permeability enhancement, fluid flow and mineral precipitation patterns: numerical models, *Geol. Soc. London,*  
882 *Spec. Publ.*, 299(1), 239–255, doi:10.1144/SP299.15, 2008.

883 Zhu, W. and Wong, T.-F.: The transition from brittle faulting to cataclastic flow: Permeability evolution, *J.*  
884 *Geophys. Res.*, 102(96), 3027–3041, doi:10.1029/96JB03282, 1997.

885

886